Variational Phase-field modeling of hydraulic fracture interaction with natural fractures and application to Enhanced Geothermal Systems

Baptiste Lepillier[1], Keita Yoshioka[2], Francesco Parisio[3], Richard Bakker[1], David Bruhn[1,4]

[1]Delft University of Technology, Stevinweg 1, Delft 2628CN, The Netherlands
[2]Department of Environmental Informatics, Helmholtz Centre for Environmental Research − UFZ, Leipzig, Germany
[3]Chair of Soil Mechanics and Foundation Engineering, Institute of Geotechnics, Technische Universität Bergakademie Freiberg, Germany
[4]GFZ German Research Centre for Geosciences, Telegrafenberg, Potsdam, Germany

Key Points:

- A novel approach for reservoir stimulation applied to an Enhanced Geothermal System.
- A robust numerical modeling of hydraulic fracture propagation and interaction with natural pre-existing fractures modeled using the variational Phase-field.
- The numerical model is applied to the field case of Acoculco geothermal reservoir.

Corresponding author: Baptiste Lepillier, b.p.lepillier@tudelft.nl

Abstract

In every tight formation reservoir, natural fractures play an important role for mass and energy transport and stress distribution. Enhanced Geothermal Systems (EGS) make no exception and stimulation aims at increasing the reservoir permeability to enhance fluid circulation and heat transport. EGS development relies upon the complex task of predicting accurate hydraulic fracture propagation pathway by taking into account reservoir heterogeneities and natural or pre-existing fractures. In this contribution, we employ the variational phase-field method which handles hydraulic fracture initiation, propagation and interaction with natural fractures and is tested under varying conditions of rock mechanical properties and natural fractures distributions. We run bi-dimensional finite element simulations employing the open-source software OpenGeoSys and apply the model to simulate realistic stimulation scenarios, each one built from field data and considering complex natural fracture geometries in the order of a thousand of fractures. Key mechanical properties are derived from laboratory measurements on samples obtained in the field. Simulations results confirm the fundamental role played by natural fractures in stimulation's predictions, which is essential for developing successful EGS projects.

1 Introduction

Interest in predicting Hydraulic Fracture propagation is picking up since the Enhanced Geothermal System (EGS) concept could become a competitive solution as a sustainable and essentially carbon-free energy resource. In EGS, the reservoir is stimulated by injecting pressurized fluids in reservoir rock formations with the aim of enhancing permeability. Early application of permeability enhancement were performed in oil and gas reservoirs (Economides & Nolte, 1989) while nowadays the principles of hydraulic fracture mechanics are applied to a broad range of problems, such as nuclear waste disposal (Zoback et al., 2003), carbon-capture storage (Fu et al., 2017), glacier dynamics (Tsai & Rice, 2010), earthquake nucleation (D. I. Garagash & Germanovich, 2012) and geothermal systems (Legarth & Saadat, 2005; McClure & Horne, 2014; Fox et al., 2013). Hydraulic fracture propagation is intrinsically a multi-scale problem (D. I. Garagash et al., 2011), with a wide range of scales of time and length controlling the fluid-driven crack propagation (Detournay, 2016). Under simplified assumptions of problem geometry and physical behavior, analytical solutions (D. Garagash & Detournay, 2000; J. I. Adachi & Detournay, 2002; Savitski & Detournay, 2002; Detournay, 2016) give good predictions of multi-scale asymptotic behavior which has been confirmed by laboratory experiments in highly controlled environments (Bunger & Detournay, 2008). Numerical methods are more computationally costly but can also overcome the simplifications typical of analytical solutions (Lecampion et al., 2018), such as planar cracks and homogeneous material properties (Bunger et al., 2013). Most numerical methods are based on Linear Elastic Fracture Mechanics (LEFM) (J. Adachi et al., 2007) and the problem of hydraulic fracture propagation has been addressed either by i) assuming planar and single mode crack propagation or ii) accounting for non-planar propagating cracks that interact with pre-existing natural fractures (Weng, 2014).

The first approach assumes the crack as a planar object splitting the material in two parts with a displacement discontinuity that evolves over time: the dimensions of the hydraulic fracture (such as its length, height and aperture) change as the fluid is injected. Models of three-dimensional (3D) bi-wing planar fractures rely upon the known fracture models from Perkins, Kern and Nordgren (PKN) (Perkins & Kern, 1961), Geertsma and de Klerk (GDK) (Geertsma & De Klerk, 1969) and more generalized three-dimensional models (Nordgren, 1972). The crack propagation criterion is based on the energy-release rate (Griffith, 1921) and propagation occurs if the stress intensity factor reaches the critical value (J. Adachi et al., 2007). Viscous dissipation of fluid is an additional source of energy dissipation in hydraulic fracturing where the LEFM solution is coupled with Poiseuille's

flow in the fracture and Carter's equation for leak-off from the fracture to the formation (Detournay & Cheng, 1993). The crack propagates along trajectories in a parametric space whose asymptotic regimes are characterized by a prevailing mechanism among leak-off, toughness, storage and viscosity (Detournay, 2016). Rock's stiffness, strength and permeability, fluid's viscosity and injection rate control the trajectories of the parametric space. Although single mode-I planar crack models give good estimates of the fracture dimensions whenever the basic assumptions hold valid, they fall short whenever heterogeneities cannot be neglected–a typical occurrence in geothermal reservoirs.

Models of fracture interaction (Warpinski & Teufel, 1987; Jeffrey et al., 1994, 2009; Renshaw & Pollard, 1995; Weng, 2014; McClure Mark et al., 2015) have to account for hydraulic fracture arrest, cross or branch at the intersection with a natural fracture (Figure 1). Although Yew & Weng (2015) report the Unconventional Fracture Model (UFM) by Weng et al. (2011) as one of the first models of hydraulic fracture propagation that accounts for fluid flow and complex network of natural fractures, several problems regarding the computational mechanics of hydraulic fracture remain unsolved. Two main approaches have so far emerged: i) the first one employs the Displacement Discontinuity Method (DDM), such as the Unconventional Fracture Model (UFM) or Crack Tip Open Displacement (CTOD) and ii) the second one uses Finite Elements or Finite Volumes Methods (FEM or FVM), where natural fractures are either smeared using an implicit approach (Non-local Damage or Phase-Field) or embedded into Cohesive Zone Models. The DDM is computationally inexpensive, as it requires discretization of the boundaries only, but cannot handle reservoir heterogeneities. The FEM with explicit embedded discontinuities faces two main drawbacks: i) it requires fine crack-tip discretization to preserve accuracy, hampering its applicability to real-case scenarios where the hydraulic fracture is expected to propagate for several hundreds of meters, and ii) it suffers from element-distortion issues that generate inaccuracies in crack opening calculations and induce numerical instabilities. The eXtended Finite Element Method (Belytschko & Black, 1999; Belytschko et al., 2001; Moës et al., 1999; Yazid et al., 2009; Gupta & Duarte, 2016; Wang, 2019) overcomes the classical finite elements limitations of resolving field discontinuities by use of enriched shape-function, although it is computationally expensive, can hardly handle *hydraulic fracture - natural fractures* interaction and can on occasions be numerically unstable.

The phase-field method of fracture is a valid and promising alternative. Given its success in modeling propagation of brittle fracture, its development has been extended to ductile (Ambati et al., 2015; Miehe, Hofacker, et al., 2015; Kuhn et al., 2016; Alessi et al., 2017), fatigue (Alessi et al., 2018; Seiler et al., 2018; Carrara et al., 2019), and dynamic fractures (Bourdin et al., 2011; Borden et al., 2012; Hofacker & Miehe, 2012; Schlüter et al., 2014; Li et al., 2016; Fischer & Marigo, 2019). The variational phase-field (V-pf) is a generalized Griffith criterion (Francfort & Marigo, 1998) numerically implemented using a phase-field variable, which smears the sharp interface fracture with a smooth transition function (Bourdin et al., 2000). The phase-field variable describes the transition from intact to fully damaged state of the material over a specific length scale. Seminal works of the application of the V-pf approach to hydraulic fracture include Bourdin et al. (2012); Chukwudozie et al. (2013) while following studies addressed problems related to poro-elasticity (Wheeler et al., 2014; Mikelić et al., 2015; Miehe, Mauthe, & Teichtmeister, 2015; Wilson & Landis, 2016; Santillán et al., 2017), fracture width computation (Xia et al., 2017; Lee et al., 2017), coupling with the theory or porous media (Ehlers & Luo, 2017; Heider & Markert, 2017), pressure dependent failure mechanisms (Choo & Sun, 2018), mass conservation (Chukwudozie et al., 2019), in-situ stresses (Shiozawa et al., 2019). The smeared representation can handle complex fracture topology where natural fractures can be represented within non-conforming discretizations, without a-priori assumptions on their geometry or restriction on hydraulic fracture growth trajectories (Yoshioka & Bourdin, 2016).

In this study, we solve the toughness dominated hydraulic fracturing problem with a V-pf approach formulated with the constitutive model known as no-tension or masonry model (Freddi & Royer-Carfagni, 2011; Del Piero, 1989). The main goal is to study the hydraulic fracture interaction with reservoir heterogeneities in the form of pre-existing natural fractures with efficient computational V-pf models. We apply the V-pf method to a real case study of a potential EGS system, i.e., the Acoculco geothermal field located in Puebla, Mexico. Two exploration wells were drilled within the geothermal field and, through log data analysis, a high temperature ($T \sim 300\,^{\circ}\mathrm{C}$) and low permeable ($k = 1 \times 10^{-18}\,\mathrm{m}^2$) reservoir was identified at $\sim 2\,\mathrm{km}$ depth. Natural fractures are modeled as complex Discrete Fracture Networks (DFN) calculated from outcrop field measurements and mechanical rock properties are derived from laboratory testing on samples collected in the field.

This article is structured as follows: in section 2, we introduce the governing equations of the V-pf model, their implementation in the open-source software OpenGeoSys (Kolditz et al., 2012), the experimental program and the stochastic method to build DFNs. In Section 3 we introduce applications of simple computational scenarios and geothermal reservoir stimulation. Section 4 presents the results of the simulations and contains a wider discussion of our results as well as broader implications of our main findings. Finally, we draw general conclusions of the study in section 6.

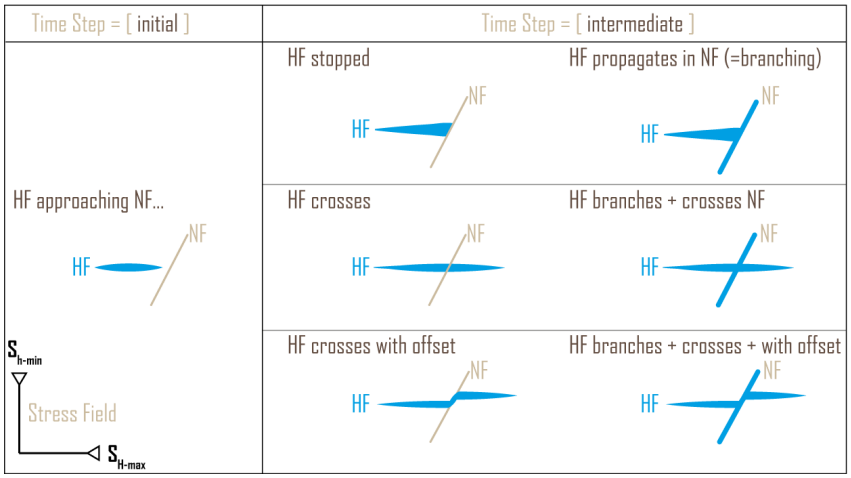

Figure 1: Possible interaction process of hydraulic fracture and natural fractures: i) Hydraulic fracture encounters a natural fracture can either arrests, cross or be deviated by the natural fracture; ii) hydraulic fracture encounters a natural fracture and propagates along its direction, which can generate branching.

2 Variational Phase-field Model

2.1 Variational approach to fracture

LEFM is based on Griffith's observation that the energy dissipation by a propagating crack equals the mechanical energy decay (Griffith, 1921). Thus the criterion for fracture propagation is given as

$$G_c = G, \tag{1}$$

where G_c is the critical surface energy release rate and G is the mechanical energy restitution rate. The energy restitution rate is defined as the derivative of the elastic energy $\mathcal{P}$ with respect to a crack increment length a, which is often derived using the concept of stress intensity factor Irwin (1957). Griffith criterion reads then as

$$\frac{\partial \mathcal{P}}{\partial a} = G_c, \tag{2}$$

which was revisited by Francfort & Marigo (1998) noticing that it can be described in terms of critical values of the following total energy along a prescribed path as

$$\mathcal{P} + G_c a. \tag{3}$$

The Griffith's criterion was generalized in the variational framework by considering a total energy with any crack set Γ as opposed to a prescribed path a as

$$\underbrace{\mathcal{F}}_{\text{Total energy}} = \underbrace{\mathcal{P}}_{\text{Mechanical energy}} + \underbrace{\int_{\Gamma} G_c \, \mathrm{d}S}_{\text{Surface energy}} , \tag{4}$$

such that the fracture propagation criterion is obtained by solving for the set of mechanical energy $\mathcal{P}$ and the crack geometry Γ that minimizes Equation (4). For a prescribed crack path (e.g., a), the approach converges to Griffith's criterion which can be viewed as a local energy minimum problem.

2.2 Governing Equations

The linear elastic constitutive equation of a brittle-elastic porous medium occupying a domain Ω can be expressed as (Biot, 1941)

$$\boldsymbol{\sigma} = \mathbf{C} : \boldsymbol{\varepsilon}(\mathbf{u}) + \alpha p_p \mathrm{I}, \tag{5}$$

where $\mathbf{C}$ is the fourth order linear elastic tangent operator, α is the Biot's coefficient, p_p is the pore-pressure, I is the identity matrix, and ε is the linearized strain tensor defined as the symmetric part of the displacement gradient $\nabla \mathbf{u}$

$$\boldsymbol{\varepsilon}(\mathbf{u}) := \frac{\nabla \mathbf{u} + \nabla \mathbf{u}^t}{2}. \tag{6}$$

Also, consider crack set Γ filled with a fluid at pressure p_f and let $\partial\Omega_{\mathrm{N}}$ be a portion of its boundary and $\partial\Omega_{\mathrm{D}} := \partial\Omega \backslash \partial\Omega_{\mathrm{N}}$ the remaining part, static equilibrium and continuity of stress at the interfaces mandates that

$$\begin{cases} \nabla \cdot \boldsymbol{\sigma}(\mathbf{u}) = \mathbf{0} & \text{in } \Omega \setminus \Gamma, \\ \boldsymbol{\sigma} \cdot \mathbf{n} = \boldsymbol{\tau} & \text{on } \partial\Omega_{\mathrm{N}}, \\ \mathbf{u} = \mathbf{u}_0 & \text{on } \partial\Omega_{\mathrm{D}}, \\ \boldsymbol{\sigma}^{\pm} \cdot \mathbf{n}_{\Gamma^{\pm}} = p_f \mathbf{n}_{\Gamma^{\pm}} & \text{on } \Gamma^{\pm}. \end{cases} \tag{7}$$

where $\mathbf{f}$ denotes an external body force and $\boldsymbol{\tau}$ is a traction force. Multiplying (7) by a test function $\delta\mathbf{u} \in H^1(\Omega \setminus \Gamma)$ that vanishes on $\partial\Omega_{\mathrm{D}}$ and using Green's theorem, we obtain

$$\int_{\Omega\setminus\Gamma} \mathbf{C}\left(\boldsymbol{\varepsilon}(\mathbf{u}) - \frac{\alpha}{N\kappa}p_p\mathrm{I}\right)\cdot\boldsymbol{\varepsilon}(\delta\mathbf{u})\,\mathrm{d}V = \int_{\partial\Omega_N^m}\boldsymbol{\tau}\cdot\delta\mathbf{u}\,\mathrm{d}S + \int_\Gamma p_f\left[\delta\mathbf{u}\cdot\mathbf{n}_\Gamma\right]\,\mathrm{d}S + \int_{\Omega\setminus\Gamma}\mathbf{f}\cdot\delta\mathbf{u}\,\mathrm{d}V, \quad (8)$$

where $N = 2$ and $N = 3$ for 2D and 3D respectively and κ denotes the material's bulk modulus. We recall that given p_p, p_f, and Γ, Equation (9) is the unique solution of the minimization among all kinematically admissible displacement of

$$\mathcal{P} = \int_{\Omega\setminus\Gamma} W\left(\boldsymbol{\varepsilon}(\mathbf{u}), p_p\right)\,\mathrm{d}V - \int_{\partial\Omega_N^m}\boldsymbol{\tau}\cdot\mathbf{u}\,\mathrm{d}S - \int_\Gamma p_f\left[\mathbf{u}\cdot\mathbf{n}_\Gamma\right]\,\mathrm{d}S - \int_{\Omega\setminus\Gamma}\mathbf{f}\cdot\mathbf{u}\,\mathrm{d}V, \quad (9)$$

where

$$W\left(\boldsymbol{\varepsilon}(\mathbf{u}), p\right) := \frac{1}{2}\mathbf{C}\left(\boldsymbol{\varepsilon}(\mathbf{u}) - \frac{\alpha}{N\kappa}p_p\mathrm{I}\right)\cdot\left(\boldsymbol{\varepsilon}(\mathbf{u}) - \frac{\alpha}{N\kappa}p_p\mathrm{I}\right), \quad (10)$$

is the poro-elastic strain energy density (Yoshioka & Bourdin, 2016).

2.3 Phase-field Approximation

The numerical implementation of the minimization of Equation (4) involves discontinuous deformation across unknown discontinuity surfaces (the cracks), Γ, which pose significant challenges in terms of numerical implementation. Instead, Equation (4) is regularized using the phase-field approach (Bourdin et al., 2000, 2008).

Introducing a scalar phase-field variable, $v : \Omega \mapsto [0, 1]$, which represents a state of the material from intact material ($v = 1.0$) to fully broken ($v = 0.0$) with a continuous function and a regularization parameter with the dimension of a length, $\ell_s > 0$, which controls the transition length of the phase-field variable, Equation (4) can be approximated as (Bourdin et al., 2012)

$$\mathcal{F}_{\ell_f} = \int_\Omega v^2 W\,\mathrm{d}V - \int_{\partial^m_N\Omega}\boldsymbol{\tau}\cdot\mathbf{u}\,\mathrm{d}S - \int_\Omega\mathbf{f}\cdot\mathbf{u}\,\mathrm{d}V + \int_\Omega p_f\,\mathbf{u}\cdot\nabla v\,\mathrm{d}V + \frac{1}{4c_n}\int_\Omega G_c\left(\frac{(1-v)^n}{\ell_s} + \ell_s|\nabla v|^2\right)\,\mathrm{d}V, \quad (11)$$

where c_n is a normalization parameter defined as $c_n := \int_0^1(1-s)^{n/2}\mathrm{d}s$. Case $n = 1$ is often referred as AT_1 ($c_n = 3/2$) and case $n = 2$ as AT_2 ($c_n = 1/2$) (Tanné et al., 2018). It can then be shown (Ambrosio & Tortorelli, 1990, 1992; Braides, 1998) that as ℓ_s approaches 0, the minimizers of Equation (11) converge to that of Equation (4) in the sense that the phase-field function v takes value 1 far from the crack Γ and transitions to 0 in a region of thickness of order ℓ_s along each crack faces of Γ.

We can observe that in Equation (11), the evolution of the phase-field (v) is driven by the strain energy (W) regardless of the deformation direction, which leads to equal strength in tension and compression – a wrong approximation for granular material such as rock. To overcome the limitation, the strain energy can be decomposed into the positive (extension) and negative (shortening) parts

$$W = W^+ + W^-. \quad (12)$$

Among the several approaches for the strain decomposition (Amor et al., 2009; Miehe et al., 2010; Freddi & Royer-Carfagni, 2011), we employ the so-called masonry model (Freddi & Royer-Carfagni, 2011), in which the material will not withstand tensile stresses.

We represent discontinuous interfaces by a diffused variable of the phase-field type (v) whose fracture toughness or cohesive strength is different from the surrounding (Fig. 2). To compensate the fracture toughness in the smeared interface $x < b$, we solve the surface energy functional in Equation (11) for the effective fracture toughness, $\tilde{G_c}^{\text{int}}$ (Hansen-Dörr et al., 2019). The surface energy equality can be imposed as

$$\tilde{G_c}^{\text{int}} \int_\Omega S \,\mathrm{d}V = G_c^{\text{int}} \int_{\xi=0}^{\xi=b} S \,\mathrm{d}V + G_c^{\text{bulk}} \int_{\xi=b}^{\infty} S \mathrm{d}V, \tag{13}$$

where

$$S = \frac{1}{4c_n} \left(\frac{(1-v)^n}{\ell_s} + \ell_s |\nabla v|^2 \right), \tag{14}$$

and ξ is the distance from the crack ($v = 0$). We built the FEM model containing natural fractures by assigning the equivalent fracture toughness computed in Equation (13) to the region within distance b from the fractures.

2.4 Numerical Implementation

We neglect leak-off to the rock mass because the permeability of the rock mass is sufficiently low. The pore-pressure p_p can be considered invariant and set as $p_p = 0$, and $p'_f = p_f - p_p$ in the governing equations. We adopt the notation $p'_f = p$ and we assume that p is spatially constant, which implies that the pressure loss within the crack is negligible. Equation (11) is solved by the alternate minimization with respect to the displacement $\mathbf{u}$ and the phase-field v with a constraint of prescribed time-evolving fluid volume which must be equal to the crack volume, i.e., $V_{\text{inj}} = V_{\text{crack}} = \int_\Omega \mathbf{u} \cdot \nabla d \,\mathrm{d}\Omega$ (Yoshioka et al., 2019). The minimisation problem can be stated as

$$(\mathbf{u}, v, p)^* = \arg\min \mathcal{F}_{\ell_f}(\mathbf{u}, d, p) \;, \quad \begin{cases} \mathbf{u} \in H^1 \\ v \in H^1, v^t \subset v^{t+\Delta t} \end{cases} \tag{15}$$

with the constrain

$$V_{\text{inj}} = \int_\Omega \mathbf{u} \cdot \nabla v \,\mathrm{d}\Omega. \tag{16}$$

The first variation of the energy functional with respect to $\mathbf{u}$ is

$$\begin{aligned} \delta \mathcal{F}_{\ell_f}(\mathbf{u}, v, p; \delta\mathbf{u}) = \frac{1}{2} \int_\Omega \boldsymbol{\varepsilon}(\delta\mathbf{u}) : \left(v^2 \mathbf{C}^+ + \mathbf{C}^- \right) : \boldsymbol{\varepsilon}(\mathbf{u}) \,\mathrm{d}\Omega \\ - \int_{\partial_{\mathrm{N}}\Omega} \boldsymbol{\tau} \cdot \delta\mathbf{u} \,\mathrm{d}\Gamma - \int_\Omega \mathbf{f} \cdot \delta\tilde{\mathbf{u}} \,\mathrm{d}\Omega + \int_\Omega p \delta\mathbf{u} \cdot \nabla v \,\mathrm{d}\Omega, \end{aligned} \tag{17}$$

where $\mathbf{C}^\pm$ is the tangent stiffness tensor

$$\mathbf{C}^\pm = \frac{\partial}{\partial \boldsymbol{\varepsilon}} \left(\frac{\partial W^\pm}{\partial \boldsymbol{\varepsilon}} \right). \tag{18}$$

The first variation of the energy functional with respect to v for AT_1 is

$$\delta\mathcal{F}_{\ell_s}(\mathbf{u},v,p;\delta v)=\int_\Omega v\delta v\,\mathbf{C}^{+}\boldsymbol{\varepsilon}(\mathbf{u})\cdot\boldsymbol{\varepsilon}(\mathbf{u})\,\mathrm{d}V+\frac{3}{8}\int_\Omega G_c\left(-\frac{\delta v}{\ell_s}+2\ell_s\nabla v\cdot\nabla\delta v\right)\,\mathrm{d}V-\int_\Omega p\,\mathbf{u}\cdot\nabla\delta v\,\mathrm{d}V, \tag{19}$$

and for AT_2 is

$$\delta\mathcal{F}_{\ell_s}(\mathbf{u},v,p;\delta v)=\int_\Omega v\delta v\,\mathbf{C}^{+}\boldsymbol{\varepsilon}(\mathbf{u})\cdot\boldsymbol{\varepsilon}(\mathbf{u})\,dV+\int_\Omega G_c\left(\frac{v-1}{\ell_s}\delta v+\ell_s\nabla v\cdot\nabla\delta v\right)\,dV-\int_\Omega p\,\mathbf{u}\cdot\nabla\delta v\,dV. \tag{20}$$

Equation (7) is linear to p and if we let the displacement solution with $p = 1.0$ be equal to $\mathbf{u}_1$, the displacement solution $p = p$ is obtained as $\mathbf{u} = p\mathbf{u}_1$ and the crack volume is

$$\int_\Omega \mathbf{u}\cdot\nabla v\,\mathrm{d}\Omega = p\int_\Omega \mathbf{u}_1\cdot\nabla v\,\mathrm{d}\Omega. \tag{21}$$

At a given time step, a volume V_{inj} is injected and equation (16) yields the mass balance in the porous medium such that the corresponding p is

$$p=\frac{V_{\mathrm{inj}}}{V_p}, \tag{22}$$

where

$$V_p=\int_\Omega \mathbf{u}_1\cdot\nabla v\,\mathrm{d}\Omega, \tag{23}$$

and the whole solution procedure is described in Algorithm 1.

Parallel simulations were run on the high-performance computing system JUWELS, maintained at the Jülich Supercomputing Centre. The total number of degree of freedom for the Acoculco case scenarios is 513 108 with 170 996 linear quadrilateral elements with a few triangular elements in the mesh resolution transition zone. Domain-decomposition was done using METIS (Karypis & Kumar, 1998) and both linear and non-linear solvers from PETSc Balay et al. (2019) were used. More specifically, the Newton–Raphson solver for the deformation problem and a Newton based variational inequality solver for the phase-field, since the phase-field solution is bounded in $[0, 1]$ domain and constrained by the irreversibility. The simulations were distributed into 384 cores over 8 nodes (Dual Intel Xeon Platinum 8168) with 2×24 cores. While the computation time differs depending on the non-linearity of each problem, all the simulations shown in the subsequent section were completed within ~ 20 h.

Algorithm 1 Incorporation of the volume constraint in the phase-field model.

repeat
  Update the injected volume, $V_{\text{inj}}(t_n + \Delta t)$
  repeat
    Solve for $\mathbf{u}_1^i$, given v^{i-1} and $p = 1.0$
    Solve for v^i, given $\mathbf{u}^i$ and $p = p^{i-1}$
    Calculate V_p^i from $\int_\Omega \mathbf{u}^i \cdot \nabla v^i \, \mathrm{d}\Omega$
    Update pressure, $p^i = V_{\text{inj}}/V_p^i$
  until $\left\| v^i - v^{i-1} \right\| < 10^{-4}$
until $V < V_{\text{final}}$

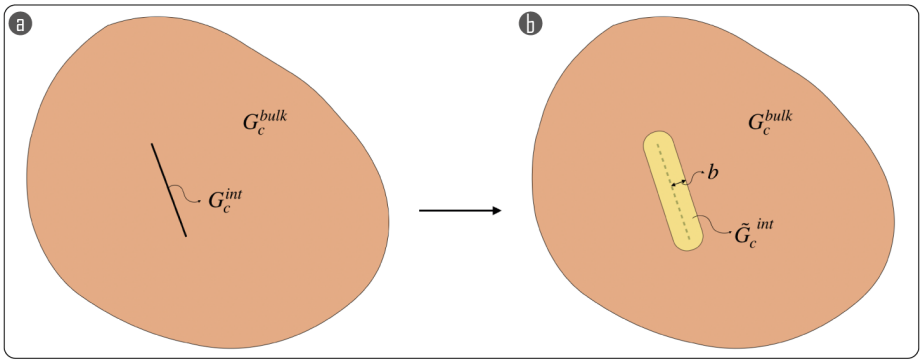

Figure 2: Diffused representation of a discontinuous interface

3 Applications

3.1 Sensitivity Analyzes

We perform a sensitivity analysis to highlight the complex interactions between fluid-driven propagating fractures and existing ones. We analyze simplified models assuming a perfectly homogeneous brittle linear elastic material containing one or two pre-existing natural fractures. We evaluate the impact on fracture initiation and propagation given by stiffness (elastic parameters) and strength (fracture toughness) of the bulk rock, existing fractures, state of stress and orientation angle of the natural fractures. The base case parameters of the sensitivity analysis are in the range of the studied rocks of the Acoculco reservoir, i.e., G_c =100 Pa m, E =25 GPa and $\nu = 0.2$.

As implemented in the V-pf, the interaction with the pre-existing natural fractures is partly controlled by the critical energy release rate of the natural fracture $\tilde{G_c}^{\text{int}}$. We compare results for $G_c = 1$ with different values of $\tilde{G_c}^{\text{int}}$ spanning four orders of magnitude, i.e., $\tilde{G_c}^{\text{int}} = 0.01, 0.05, 0.1, 10$. We analyze the impact of the far-field deviatoric stress by increasing the S_{Hmax} from 21 MPa to 60 MPa with a fixed S_{hmin} =20 MPa. All case scenarios are presented in Table 1. We finally analyze the influence of a natural fracture oriented 45° from the direction of hydraulic fracture propagation to study the effect of the incidence angle between the direction of propagation and the orientation of a natural fracture.

Table 1: Case scenarios of the sensitivity analysis with different stress fields applied. Stress values are expressed in MPa.

Case	S_{Hmax}	S_{hmin}
A	21	20
B	30	20
C	40	20
D	60	20

3.2 The Acoculco Geothermal Reservoir

In this manuscript, we analyze the potential permeability enhancement in a fractured reservoir by modeling the fracture growth from a well-bore injection. We apply the developed numerical methodology described in section 2 on the Acoculco case scenario, considering the local geological features and the rock properties gathered from field campaigns and laboratory measurements. Here we report a brief synthesis of the experimental program, field campaign, DFN construction algorithm and results, while further details can be found in the original works (Lepillier et al., 2020, 2019).

The Acoculco geothermal field, located in Mexico, hosts two vertical exploration wells (named EAC1 and EAC2) drilled at $\sim 500\,\mathrm{m}$ apart horizontally, both reaching a total depth of $\sim 2\,\mathrm{km}$ (López-Hernández et al., 2009; Canet et al., 2015; Weydt et al., 2018). On the one hand, Acoculco is considered a tight reservoir because the rock formations are little permeable ($10^{-18}\,\mathrm{m}^2$) and the fractures are scarcely connected (Lepillier et al., 2020); on the other hand, it is a suitable candidate for EGS development because of its high geothermal energy potential given that the geothermal gradient is above average ($\sim 150\,^{\circ}\mathrm{C\,km}^{-1}$). The stratigraphy encountered during drilling is simplified into three lithological units: Limestones, Marbles, Skarns. Stiffness (E and ν), strength and critical energy release rate (G_c) of the three lithologies were measured in the rock physics laboratory. Young's modulus and Poisson's ratio were determined by Unconfined Compression Strength (UCS) tests (UCS - 20 experiments). Brazilian disc (BD - 80 experiments) and Chevron Bend tests (CB - 12 experiments) were employed to determine the fracture toughness K_{Ic} of the rock formations, which was later employed to derive the critical energy release rate (G_c). Fracture toughness was determined from the two sets of experiments: i) from BD tests, it was done following the method proposed by Guo et al. (1993) and ii) for CB tests, following the method suggested by Franklin et al. (1988). All material parameters employed in the model are summarized in Table 2.

Table 2: Rock mechanical properties from rock physics laboratory measurements. This table summarizes the main results of the laboratory measurements for the concerned lithologies: Limestones, Marbles and Skarns. For each of them the table gives: the Young's modulus (E), the Poisson's ratio (ν), the fracture toughness (K_{Ic}), and Griffith's critical energy release rate (G_c). A single final value for specific lithology was selected as the average between different locations outcrops.

Lithology	E GPa	ν -	K_{Ic} MPa m$^{1/2}$	G_c Pa m
Limestone Late Cretaceous	37.8	0.31	2.76	201
Limestone Early Cretaceous	37.9	0.23	2.49	164
Limestone	**37.9**	**0.27**	**2.63**	**182**
Marble from Pueblo Nuevo	46.8	0.25	1.90	77.3
Marble from Tatatila	51.6	0.29	1.85	66.2
Marble	**49.2**	**0.27**	**1.87**	**71.4**
Exo-skarn from Eldorado	56.9	0.11	2.70	127
Endo-skarn from Boquillas	41.1	0.13	1.92	89.3
Skarn	**49.0**	**0.13**	**2.31**	**108**

The general DFN is derived from scanline measurements from multiple outcrops analogues of the Acoculco geothermal system (Lepillier et al., 2020) that are later extrapolated using the multiple point statistic method (Bruna et al., 2019). The method yields three separate DFNs, i.e., one per lithology. Each one of the three DFNs is a bi-dimensional geo-referenced section of $600 \times 600\,\mathrm{m}^2$ (fig. 3). Some further processing is necessary to build the FEM models. In the first step, we extracted from each DFN a smaller sub-domain of $100 \times 100\,\mathrm{m}^2$ (Figure 3). Each extraction has a specific fracture distribution: to analyze the impact of stimulating one or another specific section of the domain. In the second step we extracted an additional three sub-domain from each of the DFNs. The three sub-DFNs, one for each DFN, are then rotated in the third step to align the maximum horizontal stress S_{Hmax} with the x-axis and further down-scaled in the fourth step to fit the a-dimensional V-pf formulation.

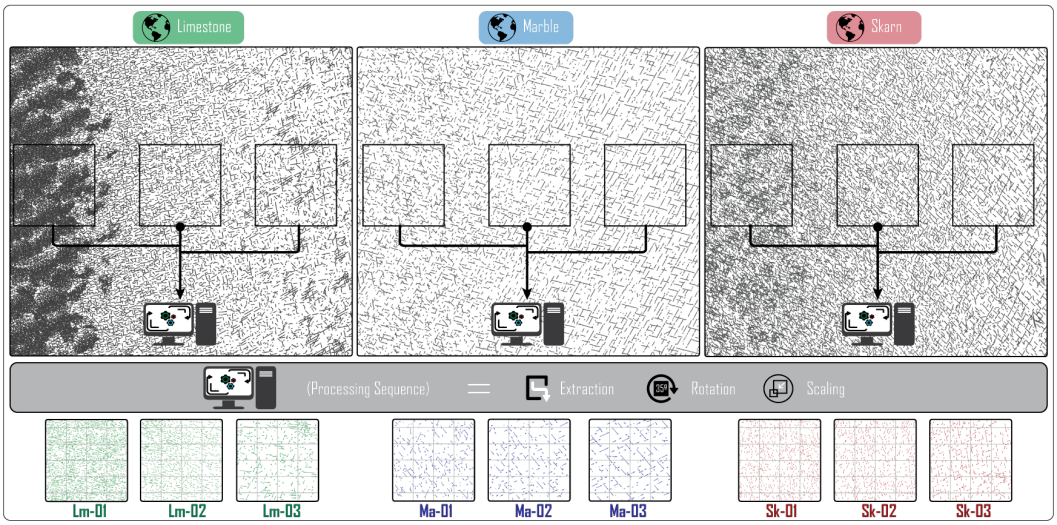

Figure 3: This figure presents the pre-processing sequence: from original reservoir scale DFN, to extracted, rotated and scaled models to fit the numerical analyzes requirements. From left to right, the DFN for the Limestone formation, the DFN for the Marble formation and the DFN for the Skarn formation. Symbols Lm/Ma/Sk-01,-02,-03 are referred to the sub-DFN extracted from initial DFN.

The in-situ stress state is believed to be of the normal faulting type and the orientation of the stress tensor is taken from the World Stress Map (Lepillier et al., 2019; Heidbach et al., 2016). Based on this assumption, having $sv > shmax > shmin$, we defined certain values for S_{Hmax} and S_{hmin}. In normal-faulting regime, the hydraulic fracture propagates along the vertical plane oriented perpendicular to S_{hmin}. Because of this, we assume 2-dimensional plane-strain conditions were we assign only S_{Hmax} and S_{hmin}.

4 Results

4.1 Sensitivity Analysis

Figure 4 shows the influence of strength (G_c) and stiffness (E and ν) on the internal fracture over-pressure and length evolution during hydraulic fracture propagation at constant fluid injection-rate. The critical energy release rate G_c is the dominant parameter controlling the hydraulic fracture response (fig. 4a): G_c represents the resistance to fracture propagation, hence is proportional to the maximum overpressure reached and inversely proportional to the rate of crack length growth during injection. The stiffness parameters play a smaller role on the problem evolution, and, whilst the influence of Poisson's ratio seems to be negligible over the selected range (Figure 4c), an increase in Young's modulus entails an increase in fracture propagation resistance (fig. 4b). Maximum overpressure is proportional to Young's modulus and inversely proportional to the injected volume at propagation onset.

The delay in crack propagation onset is a consequence of lower stiffness: the more the rock is compliant, the larger the volume of fluid needs to be injected before the crack internal pressure reaches the propagation condition and the energy release rate equals its critical value. Globally, it can be interpreted as a higher system compressibility, where more compliant systems require higher volume of injected fluids.

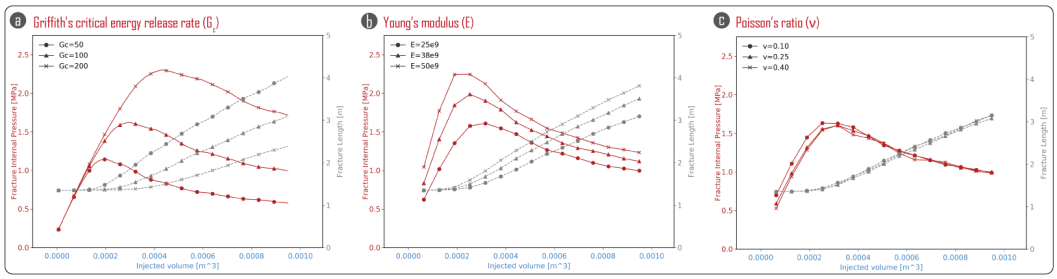

Figure 4: Sensitivity analysis of mechanical material properties. The plots report the evolution of fracture internal over-pressure (reds) and fracture length (greys) against the injected volume: in (a) for different values of the critical energy release rate of the bulk solid $G_c = 50, 100, 200 \text{Pa}\,\text{m}^{-1}$; in (b) for different elastic parameters of Young's modulus with $E = 25, 38, 50\,\text{GPa}$; and (c) different Poisson's ratio $\nu = 0.10, 0.25, 0.40$.

Figure 5 shows results of the sensitivity analysis of the interaction between a fluid-driven fracture (the phase-field) and two natural fractures at equivalent time steps. When the contrast between bulk rock and natural fractures in terms of G_c is high, i.e., for relatively low $\tilde{G}_c^{\text{int}}$, the fracture propagates within the bulk rock before interacting with the natural fractures (fig. 5) as for $\tilde{G}_c^{\text{int}} = 0.01$ and $\tilde{G}_c^{\text{int}} = 0.05$. Once it propagates within the vertical natural fractures, it then turns into two sub-vertical wing-type cracks. For $\tilde{G}_c^{\text{int}} = 0.1$, the natural fractures do no have low enough strength and are crossed by the hydraulic fracture without branching (fig. 5). For $\tilde{G}_c^{\text{int}} > G_c$, the natural fracture act as a barrier to the hydraulic fracture. After the crack hits the natural fracture, it propagates in a path avoiding the natural fracture. In this case, the natural fracture acts as a barrier, shielding the hydraulic fracture propagation. Note that branching in general is energetically more expensive (less favored) but does happen when the surface energy of the natural fractures are so low that crack propagation along them becomes more attractive.

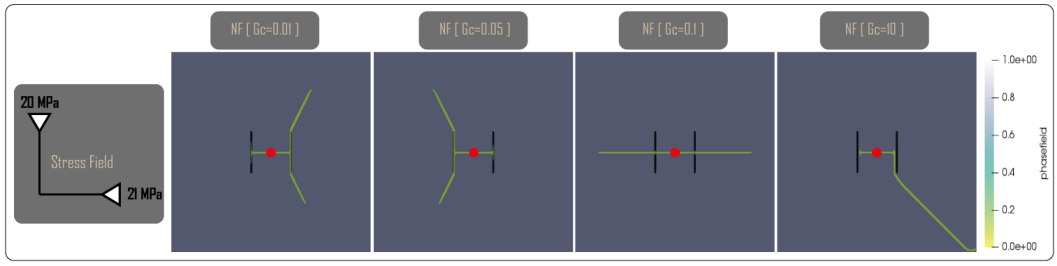

Figure 5: Sensitivity analysis of the influence of two vertical natural fractures. The results show the phase-field distribution contour map in the domain at the same time step for a constant stress field and different critical energy release rate of the natural fracture $\tilde{G}_c^{\text{int}}$. The stress field is oriented such that S_{Hmax} is aligned along the horizontal direction. The red dots represents the well-bore and initial fracture position (and initial phase-field implementation)

At increasing values of differential stress (fig. 6), and for fixed $\tilde{G}_c^{\text{int}} = 0.01$, the branching observed at low deviatoric stress disappears for $S_{Hmax} \geq 30\,\text{MPa}$. The critical stress intensity factor at the tip of the natural fracture is proportional to the hor-

izontal stress and propagating a fracture parallel to S_{Hmax} through the bulk rock requires less energy than propagating it through the vertical natural fracture. Therefore, with higher deviatoric stress, considering a natural fracture oriented 90° will not change the propagation direction as the stress dictates the propagation direction.

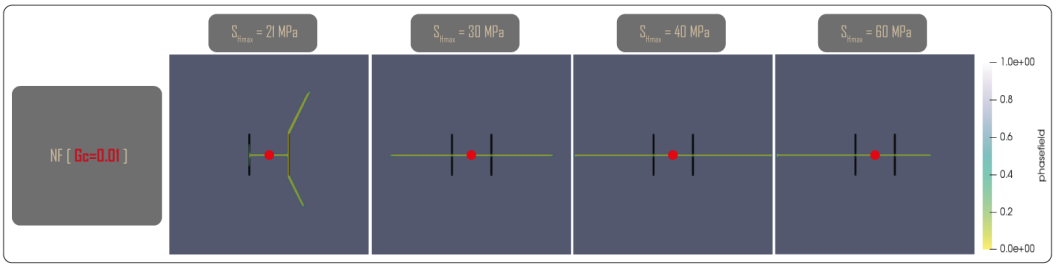

Figure 6: Sensitivity analysis of the influence of two vertical natural fractures. The results show the phase-field distribution contour map in the domain at the same time step for a constant critical energy release rate of the natural fracture $\tilde{G}_c^{\,\mathrm{int}}$ and different stress field values $\tilde{G}_c^{\,\mathrm{int}} = 0.01$. The stress field is oriented such that S_{Hmax} is aligned along the horizontal direction. The red dots represents the well-bore and initial fracture position (and initial phase-field implementation)

A 45°-oriented fracture has an orientation which is closer to the critical one for the given state of stress, hence it influences the propagation and interaction regime differently than vertical natural fracture (fig. 7). With only one natural fracture present, the problem is intrinsically asymmetric. At $\tilde{G}_{\mathrm{c}}^{\,\mathrm{int}} = 0.01$, the hydraulic fracture first interacts with the natural fracture and later propagates in the direction of S_{Hmax} (fig. 7a) and at $\tilde{G}_{\mathrm{c}}^{\,\mathrm{int}} = 0.1$, the hydraulic fracture propagation is still attracted by the inclined natural fracture but not as much as the case with $\tilde{G}_{\mathrm{c}}^{\,\mathrm{int}} = 0.1$. For high values of the natural fractures' critical energy release rate, i.e., for $\tilde{G}_{\mathrm{c}}^{\,\mathrm{int}} = 10$, even though the natural fracture is more favorably oriented, it becomes once again a barrier to fracture propagation (fig. 7a). For $\tilde{G}_{\mathrm{c}}^{\,\mathrm{int}} = 0.01$ with varying horizontal stresses S_{Hmax}, the hydraulic fracture propagation along the natural fracture is progressively hindered with increasing S_{Hmax} (fig. 7b). At $S_{Hmax} = 40\,\mathrm{MPa}$, the hydraulic fracture shows a small offset at the natural fracture's crossing point while the hydraulic fracture becomes agnostic to the natural fracture with $S_{Hmax} = 60\,\mathrm{MPa}$.

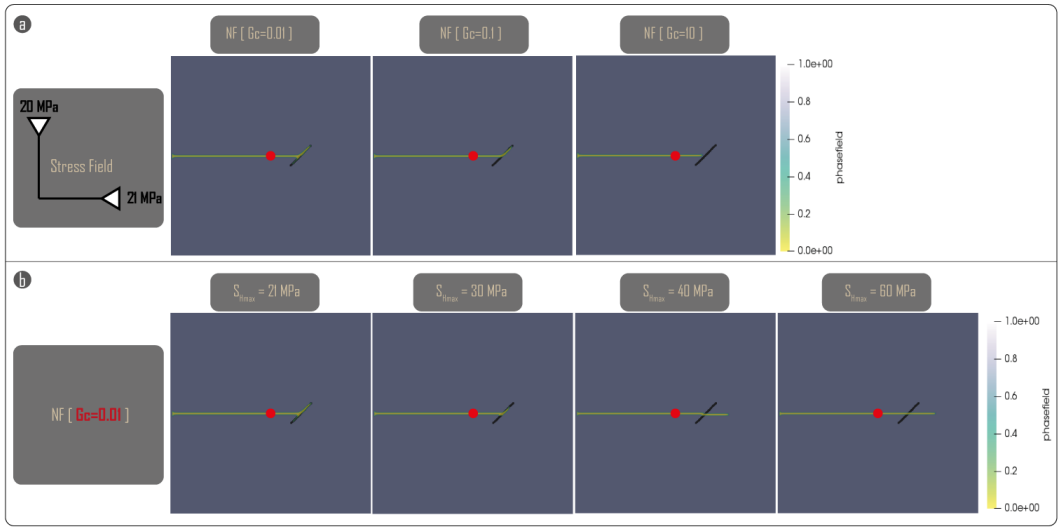

Figure 7: Sensitivity analysis of the influence of one natural fracture inclined at 45° from the horizontal axis. The results show: (a) the phase-field distribution contour map in the domain at the same time step for a constant stress field and different critical energy release rate of the natural fracture $\tilde{G}_c^{\text{int}}$; and in (b) for different values of the stress field and a constant critical energy release rate of the natural fracture $\tilde{G}_c^{\text{int}} = 0.01$ (b). The stress field is oriented such that S_{Hmax} is aligned along the horizontal direction. The red dots represents the well-bore and initial fracture position (and initial phase-field implementation)

4.2 Stimulation of the Acoculco Geothermal Reservoir

Figures 8, 9 and 10 show the results of the stimulation scenarios in the Acoculco geothermal reservoir for the different lithologies and for different DFNs. On the left of all figures is plotted the fracture pressure and length with injected volume, while on the right is shown the contour map of the phase-field along with the distribution of natural fractures. For all the cases, the propagation pressure decreases with injected volume as the crack length increases. The pressures started declining rapidly from the onset of the injection/stimulation. This is because the simulations were initiated with a borehole without setting a priori (initial) fracture lengths, as often done in practice, which led to the high breakdown pressures. Such high pressure responses may not be observed in fields because: 1) the borehole intersects with pre-existing fractures or defects or 2) the borehole is completed with perforations or well production packers. However, if fracture is initiated in a intact rock, this level of high pressure should be expected. The fracture length increment with time shows a burst-like behavior: whenever the hydraulic fracture interacts with a natural fracture, the pressure drops as a consequence of the increase in available fluid storage capacity given by the crack sudden propagation over a finite distance within the natural fracture.

Considering all lithologies, the final fracture length ranges between $\sim 75\,\text{m}$ to $\sim 95\,\text{m}$ and a the lowest propagation pressure is observed for the Marble stimulation cases (fig. 9), whilst the highest propagation pressure is observed for the stimulation into the Limestone formation (fig. 8)–a result in agreement with the sensitivity analysis.

Figure 11 shows a polar representation of the hydraulic fracture deviation from the x direction during propagation. The Limestone simulations show the larger range of fracture lengths spanning from $\sim 75\,\text{m}$ to $\sim 95\,\text{m}$ while the Marble's one have the small-

est range, spanning from $\sim 78\,\text{m}$ to $\sim 79\,\text{m}$. The angular deviation ranges in an interval of 20° above and below the reference axis given by S_{Hmax} direction. Maximum deviations are observed in Marble and Skarn simulations, reaching 30° in both simulations, while the deviation angle for the Limestone simulations is contained in a 20° interval.

The asymmetrical propagation of hydraulic fracture from the borehole is a consequence of the intersection angle between natural fracture and the approaching hydraulic fracture. Assuming θ as the angle between a natural fracture and the S_{Hmax} axis, we observed that: i) low-θ natural fracture act as pathways for the hydraulic fracture, which propagates faster along natural fractures; ii) high-θ natural fracture ($\sim 90°$) are by-passed by the hydraulic fracture and no interaction takes place. Intermediate values of θ offer a pathway for hydraulic fracture to propagate along a certain distance, until the pressure build-up is sufficiently high to allow further propagation within in the matrix.

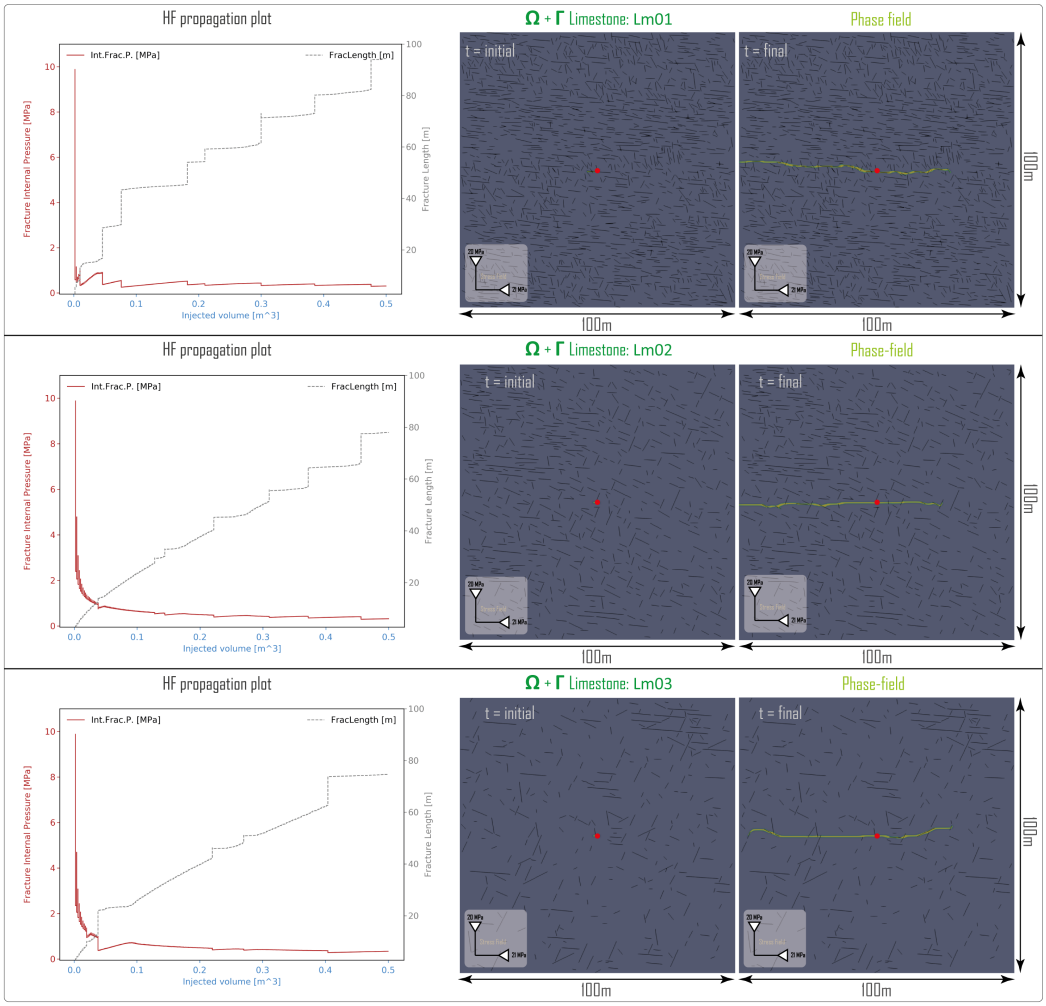

Figure 8: Hydraulic fracture models using V-pf with the sub-DFN of the Limestone reservoir. The matrix material domain Ω is represented in grey, the natural fracture Γ are discretized in black. Lm01 is composed with 1483 natural fractures, Lm02 is composed with 709 natural fractures, Lm03 is composed with 327 natural fractures. The stress field is oriented such that S_{Hmax} is aligned along the horizontal direction. The red dots represent the well-bore and initial fracture position (and initial phase-field implementation)

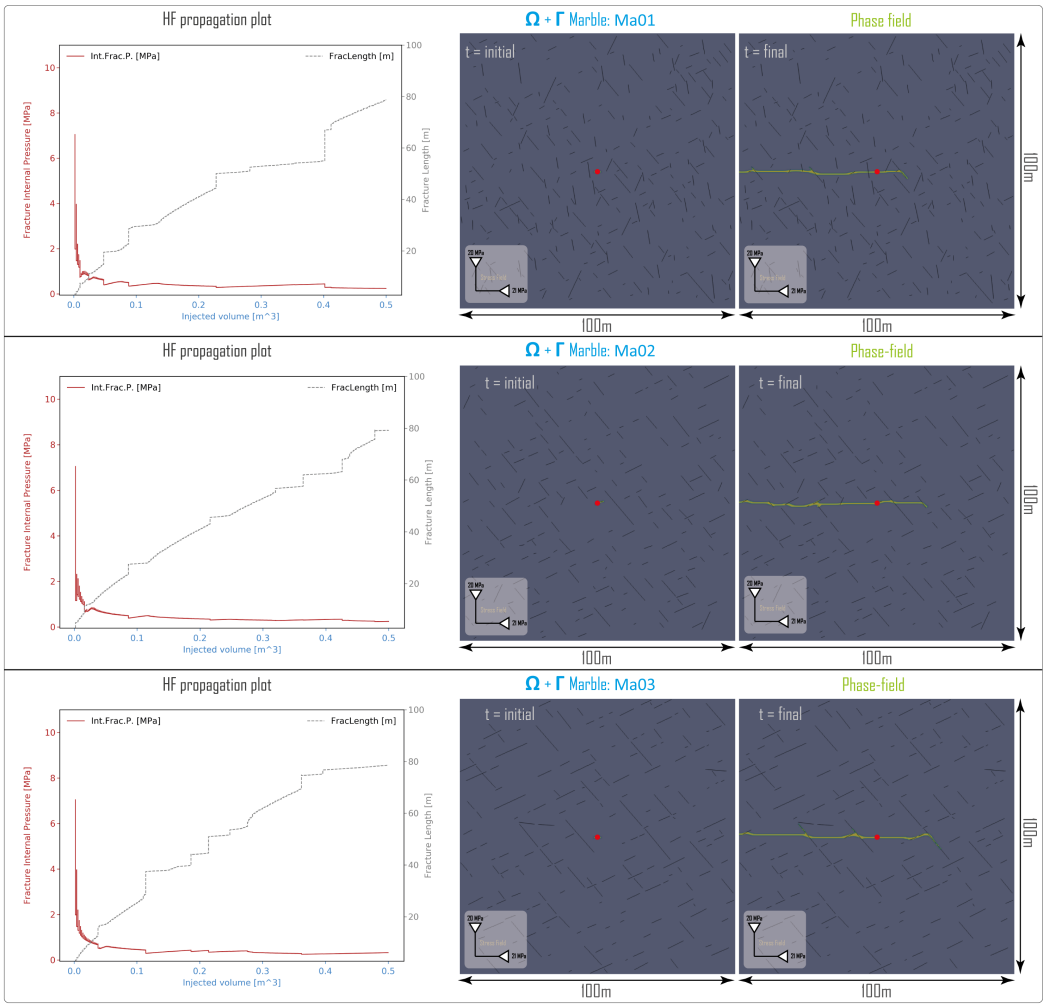

Figure 9: Hydraulic fracture models using V-pf with the sub-DFN of the Marble reservoir. The matrix material domain Ω is represented in grey, the natural fractures Γ are discretized in black. Ma01 is composed with 295 natural fractures, Ma02 is composed with 215 natural fractures, Ma03 is composed with 198 natural fractures. The stress field is oriented such that S_{Hmax} is aligned along the horizontal direction. The red dots represent the well-bore and initial fracture position (and initial phase-field implementation)

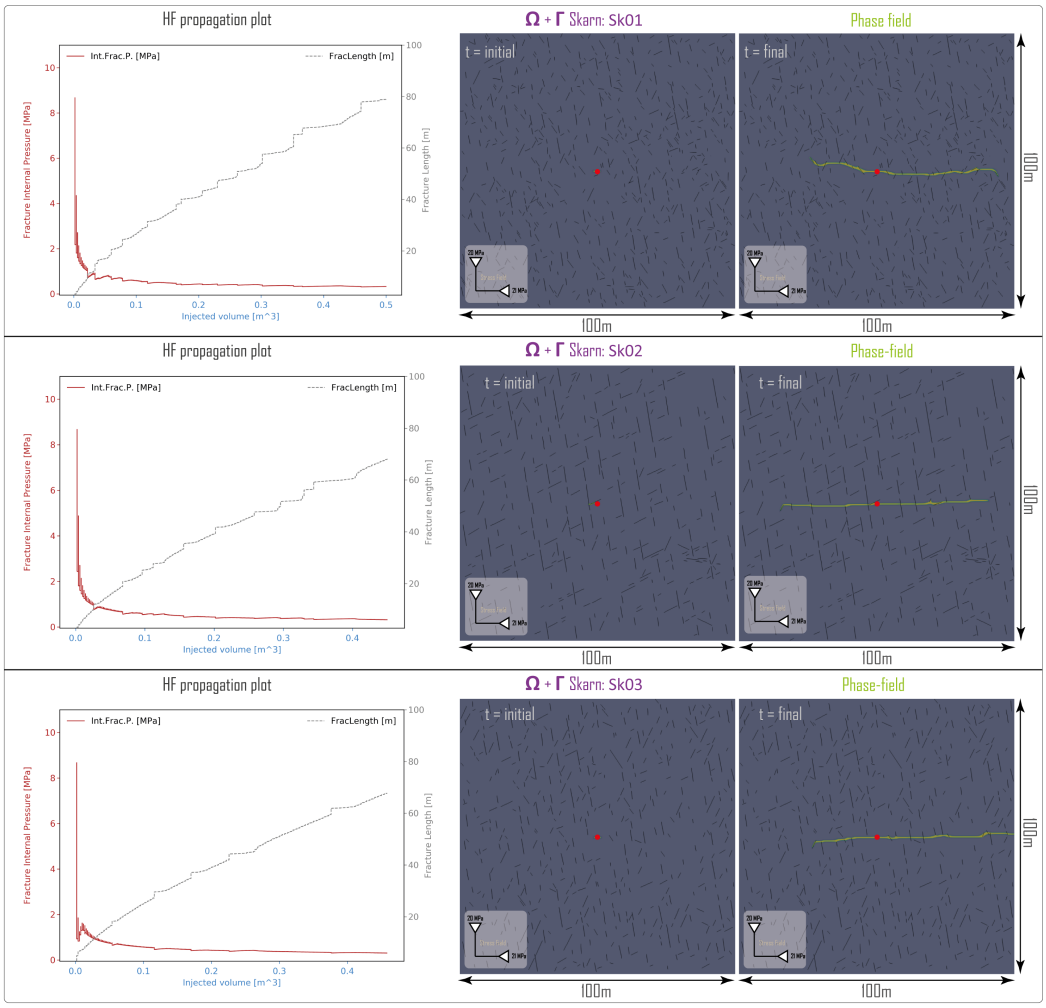

Figure 10: Hydraulic fracture models using V-pf with the sub-DFN of the Skarn reservoir. The martix material domain Ω is represented in grey, the natural fractures Γ are discretized in black. Sk01 is composed with 706 natural fractures, Sk02 is composed with 495 natural fractures, Sk03 is composed with 375 natural fractures. The stress field is oriented such that S_{Hmax} is aligned along the horizontal direction. The red dots represent the well-bore and initial fracture position (and initial phase-field implementation)

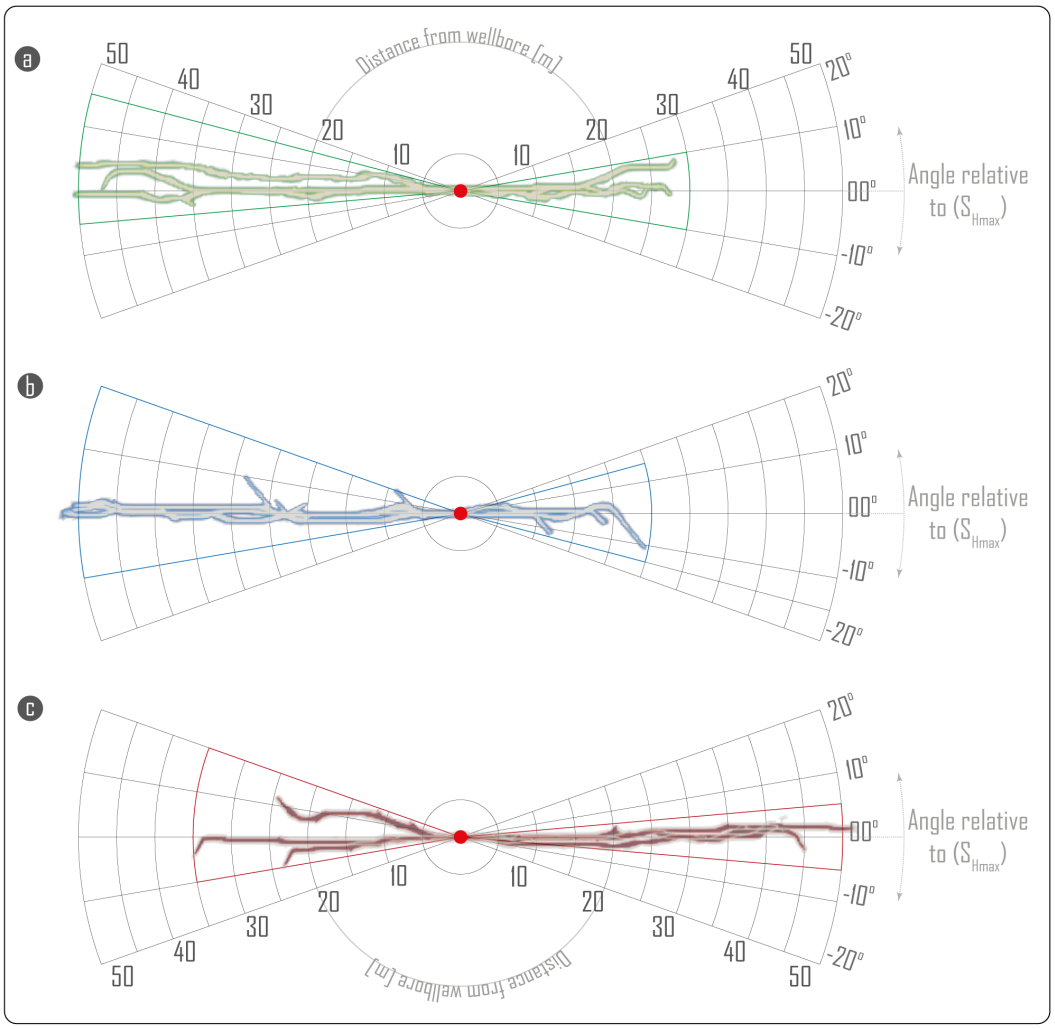

Figure 11: A comparison of hydraulic fracture simulation V-pf models for : a) the Limestones (green color); b) the Marbles (blue color); c) the Skarns (red color); hydraulic fracture lengths are given by the concentric dividers, and hydraulic fracture angles compared to S_{Hmax}'s orientation is given by the radial dividers.

5 Discussion

The V-pf method presented here is an implicit smeared approach which represents the fracture with a smoothly transitioning function that spans from intact to fully damaged state of the material. Natural fractures are represented in a non-conforming mesh with the reduced fracture toughness by enforcing energetic equivalence, which is one of the advantages of the method since it allows exploring multiple DFNs scenarios with a single discretization. As presented in this study, the ability of the V-pf is to handle complex fracture topologies with a unified criteria – energy minimization – that seeks for an admissible displacement and a set of fracture geometry that minimizes the total energy without a need for ad-hoc criteria for branching or turning. The model exhibits asymmetric crack growth under some circumstances: the phenomenon is intrinsic to the variational approach, where the energy minimization leads to the occurrence of asymmetric solutions whenever the total energy of the system is smaller than its symmetric counterpart (Gao & Rice, 1987; Bunger et al., 2008; Tanne, 2017).

The interaction behavior between hydraulic fracture and natural fractures depends: i) on the combination of the critically energy release rate ratio between natural fractures and bulk rock ($\tilde{G_c}^{int}/G_c$); ii) on the natural fractures orientation relative to the stress field; and iii) on the magnitude of principal stress components. Natural fractures can either favor or hamper the propagation of a hydro-fracture according to specific combinations of the input parameters. Natural fractures attract hydraulic fractures for relatively low values of critical energy release rate ratio, when they have orientations close to the critical ones and for relatively isotropic stress states. Natural fractures can be an obstacle to hydraulic fracture growth whenever the fracture resistance becomes higher than the one of the intact rock. Although counter-intuitive, the presence of higher strength discontinuities is a relatively frequent occurrence in deep geothermal systems: the environmental conditions could enhance geochemical reactions of dissolution and precipitation (Singurindy & Berkowitz, 2005; Watanabe et al., 2020), such as silica precipitation (Scott & Driesner, 2018; Lu et al., 2018), and the existence of active volcanism could favor the presence of magmatic intrusions even at shallow depth (Elders et al., 2014) which, if old and cold enough, could represent higher strength and stiffness bodies.

In our analyzes, we have assumed a low permeability that is typical of poorly fractured crystalline rock, an hypothesis that entails no leak-off between the fracture and the porous rock. Such an assumption is equivalent to an undrained response where the change in effective stress within the porous rock is null during injection. Although the fracture toughness (critical energy release rate) is more predominant in controlling propagation conditions when compared to stiffness, Young's modulus of the rock also plays a role. In particular, a more compliant rock requires higher injected volumes, but overall generates lower over-pressure. On the contrary, stiff rocks generate higher over-pressure for a lower injected volume. Because of the high fracture strength, high stiffness and low permeability of basement crystalline rocks, during stimulation of a deep geothermal reservoir high over-pressure can be achieved with relatively low values of injected volume (Ellsworth et al., 2019).

The V-pf simulations of the Acoculco reservoir highlighted a fluctuation in the pressure and crack-length response in time, with intermittent crack advancement and burst-like behavior–a phenomenon observed during several hydraulic stimulations (Milanese et al., 2016). The V-pf implementation adopted is numerically stable and provides continuous pressure-volume response in absence of viscous flow dissipation. The intermittent advancements are a direct consequence of the interaction between existing fractures with lower crack resistance and the fluid driven crack: whenever the hydraulic fracture encounters a natural fracture, if the latter is favorably oriented, the hydraulic fracture encounters almost no resistance and propagates rapidly over a finite length. The pressure drop is associated with a stress release in the rock, which in combination with the crack length increment, can be associated with micro-earthquakes. Micro-seismicity has been widely observed during hydraulic fracturing (Davies et al., 2013; Schultz et al., 2015; Lopez-Comino et al., 2017) and our results suggest that, in crystalline reservoirs, the phenomenon is associated with hydraulic fractures propagating along pre-existing natural fractures.

Results show that the Marble formation in the Acoculco reservoir is the optimal one for a potential stimulation because the lowest values of propagation over-pressure. The orientation of the natural fractures controls the propagation extent and direction independently of the lithology and the fracture topology dominates the hydraulic fracture response in all cases analyzed. In the present case study we have analyzed homogeneous rock matrix properties, although a more realistic approach should be based on representing fluctuation of the material properties within the rock matrix. Three-dimensional analyzes would be an additional improvement of the current scenarios. Nonetheless, the additional complexity of a three-dimensional reservoir model should be justified by a sufficient knowledge of the reservoir's structure and its property–a current shortcoming for

the Acoculco reservoir. Although a normal fault regime is likely at Acoculco reservoir and hydraulic fractures are expected to propagate mainly vertically, there are indications that a strike-slip faulting system could also be active (Liotta et al., 2020), making the full three-dimensional propagation topology rather complex and difficult to estimate a-priori.

There is current uncertainty about the in-situ state of stress at the Acoculco geothermal reservoir and different values of the stress components could yield a different output in terms of hydraulic fracture propagation. Although the DFNs that are built from outcrop extrapolations are also a source of additional uncertainty, the small prominence of fractures in the DFNs seems to be in good agreement with the very low permeability that was observed during well logging: small and poorly connected fractures hamper fluid flow in the tight reservoir.

Stimulating a highly fractured zone of the Acoculco geothermal reservoir requires a lower stimulation pressure, therefore reducing the drilling costs. Additionally, according to the well temperature measurements, the Marble and Skarn formations are more likely to be targeted for stimulation because they are present at a higher depth and therefore, they are at a higher temperature. The formation breakdown pressure is lower for the Marble, which also has a lower density of natural fractures. Nonetheless, the natural fractures in the Marble are longer and better connected when compared to the ones in the Skarn, which are shorter but more frequent. A trade-off arises between the objective of stimulating the hotter formations of the reservoir on the one hand, and stimulating the formations that would yield a longer propagation of the hydraulic fracture on the other hand. The optimal solution would depend on the ultimate goals of the EGS development and a detailed cost-balance analysis is necessary to optimize the stimulation depth.

6 Conclusions

We have presented a method for modeling hydraulic fracture propagation and interaction with a network of natural fractures in a geothermal reservoir. The fracture simulations are based on a variational phase-field approach that proved high numerical stability. We have highlighted the main factors controlling the hydraulic fracture propagation and its interaction with natural fractures through sensitivity analyzes on simplified models. We have applied the method to model a realistic EGS stimulation scenario of the geothermal reservoir of Acoculco, Mexico. The numerical model is built from field data and model parameters are derived from laboratory experiments.

Building a realistic DFN is an essential piece of the puzzle for numerical analyzes of stimulation of complex reservoirs, which can lead to counter-intuitive findings of the propagation mechanisms as opposed to simplified models of single-oriented crack families. Pressure fluctuations and burst-like crack propagation are intrinsically connected to the presence of the complex network of natural fractures.

The numerical model is implemented in the open-source software OpenGeoSys (`www.opengeosys.org`), which can be freely downloaded at `https://github.com/ufz/ogs`. We provide a working methodology for the study of EGS systems and the feasibility analyzes of hydraulic stimulation of geothermal reservoirs.

Acknowledgments

This work is part of the GEMex consortium, a European-Mexican collaboration, which aims at investigating non-conventional geothermal systems: i) an enhanced geothermal system, as studied in the case of Acoculco site; ii) and a supercritical system, as studied in the geothermal field of Los Humeros. We would like to thank all the GEMex team, and especially our Mexican partners who guided us in the field. GEMex has received fund-

ing from the European Unions Horizon 2020 research and innovation programme under grant agreement No. 727550 and the Mexican Energy Sustainability Fund CONACYT-SENER, project 2015-04-268074. More information is available on: www.gemex-h2020.eu.

K.Y. gratefully acknowledges the funding provided by the German Federal Ministry of Education and Research (BMBF) for the GeomInt project, Grant Number 03G0866A, within the BMBF Geoscientific Research Program "Geo:N Geosciences for Sustainability". The contribution of F.P. was funded by the Deutsche Forschungsgemeinschaft (DFG, German Research Foundation) project number PA 3451/1-1.

Laboratory works who not have been possible without help and support from the laboratory staff. B.L., R.B. and D.B. give thanks to the Delft University of Technology GSE laboratory staff.

The authors gratefully acknowledge the Earth System Modeling Project (ESM) for funding this work by providing computing time on the ESM partition of the supercomputer JUWELS at the Jlich Supercomputing Centre (JSC)

The datasets generated during and/or analyzed during the current study are available in the repository:
`https://doi.org/10.6084/m9.figshare.12033624.v2`

References

Adachi, J., Siebrits, E., Peirce, A., & Desroches, J. (2007). Computer simulation of hydraulic fractures. *International Journal of Rock Mechanics and Mining Sciences*, *44*(5), 739–757. doi: 10.1016/j.ijrmms.2006.11.006

Adachi, J. I., & Detournay, E. (2002). Self-similar solution of a plane-strain fracture driven by a power-law fluid. *International Journal for Numerical and Analytical Methods in Geomechanics*, *26*(6), 579–604.

Alessi, R., Marigo, J. J., Maurini, C., & Vidoli, S. (2017). Coupling damage and plasticity for a phase-field regularisation of brittle, cohesive and ductile fracture: One-dimensional examples. *International Journal of Mechanical Sciences*, 1–18. Retrieved from `http://dx.doi.org/10.1016/j.ijmecsci.2017.05.047` doi: 10.1016/j.ijmecsci.2017.05.047

Alessi, R., Vidoli, S., & De Lorenzis, L. (2018). A phenomenological approach to fatigue with a variational phase-field model: The one-dimensional case. *Engineering Fracture Mechanics*, *190*, 53–73. Retrieved from `https://doi.org/10.1016/j.engfracmech.2017.11.036` doi: 10.1016/j.engfracmech.2017.11.036

Ambati, M., Gerasimov, T., & De Lorenzis, L. (2015). Phase-field modeling of ductile fracture. *Computational Mechanics*, *55*(5), 1017–1040. Retrieved from `http://dx.doi.org/10.1007/s00466-015-1151-4` doi: 10.1007/s00466-015-1151-4

Ambrosio, L., & Tortorelli, V. M. (1990). Approximation of functional depending on jumps by elliptic functional via Γ convergence. *Communications on Pure and Applied Mathematics*, *43*(8), 999–1036.

Ambrosio, L., & Tortorelli, V. M. (1992). On the approximation of free discontinuity problems. *Boll. Un. Mat. Ital. B (7)*, *6*(1), 105–123.

Amor, H., Marigo, J.-j., & Maurini, C. (2009). Regularized formulation of the variational brittle fracture with unilateral contact: numerical experiments. *Journal of Mechanics and Physics of Solids*, *57*(8), 1209–1229. doi: 10.1016/j.cardiores.2006.11.005

Balay, S., Abhyankar, S., Adams, M., Brown, J., Brune, P., Buschelman, K., ... Zhang, H. (2019). {*PETS*}*c Users Manual* (Tech. Rep. No. ANL-95/11 - Revision 3.11). Argonne National Laboratory.

Belytschko, T., & Black, T. (1999). Elastic crack growth in finite elements with minimal remeshing. *International Journal for Numerical Methods in Engineering*, *45*(5), 601–620. doi: 10.1002/(SICI)1097-0207(19990620)45:5⟨601::AID-NME598⟩3.0.CO;2-S

Belytschko, T., Moës, N., Usui, S., & Parimi, C. (2001). Arbitrary discontinuities in finite elements. *International Journal for Numerical Methods in Engineering*, *50*(4), 993–1013. doi: 10.1002/1097-0207(20010210)50:4⟨993::AID-NME164⟩3.0.CO;2-M

Biot, M. A. (1941). General Theory of Three-Dimensional Consolidation. *Journal of Applied Physics*, *12*(2), 155–164.

Borden, M. J., Verhoosel, C. V., Scott, M. A., Hughes, T. J. R., & Landis, C. M. (2012). A phase-field description of dynamic brittle fracture. *Computer Methods in Applied Mechanics and Engineering*, *217-220*, 77–95. Retrieved from `http://dx.doi.org/10.1016/j.cma.2012.01.008` doi: 10.1016/j.cma.2012.01.008

Bourdin, B., Chukwudozie, C., & Yoshioka, K. (2012). A variational approach to the numerical simulation of hydraulic fracturing. *Proceedings - SPE Annual Technical Conference and Exhibition*, *2*, 1442–1452. doi: 10.2118/159154-ms

Bourdin, B., Francfort, G. A., & Marigo, J.-J. (2000). Numerical experiments in revisited brittle fracture. *J. Mech. and Phys. of Solids*, *48*(4), 797–826.

Bourdin, B., Francfort, G. A., & Marigo, J.-J. (2008). The variational approach to fracture. *Journal of Elasticity*, *91*(1-3), 5–148.

Bourdin, B., Larsen, C. J., & Richardson, C. L. (2011). A time-discrete model for dynamic fracture based on crack regularization. *International Journal of Fracture*, *168*(2), 133–143. doi: 10.1007/s10704-010-9562-x

Braides, A. (1998). *Approximation of Free-Discontinuity Problems* (No. 1694). Springer. Retrieved from `http://www.springerlink.com/content/978-3-540-64771-3/`

Bruna, P. O., Straubhaar, J., Prabhakaran, R., Bertotti, G., Bisdom, K., Marietho z, G., & Meda, M. (2019). A new methodology to train fracture network simulation using multiple-point statistics. *Solid Earth*, *10*(2), 537–559. doi: 10.5194/se-10-537-2019

Bunger, A. P., & Detournay, E. (2008). Experimental validation of the tip asymptotics for a fluid-driven crack. *Journal of the Mechanics and Physics of Solids*, *56*(11), 3101–3115.

Bunger, A. P., Gordeliy, E., & Detournay, E. (2013). Comparison between laboratory experiments and coupled simulations of saucer-shaped hydraulic fractures in homogeneous brittle-elastic solids. *Journal of the Mechanics and Physics of Solids*, *61*(7), 1636–1654.

Bunger, A. P., Jeffrey, R. G., & Detournay, E. (2008). Evolution and morphology of saucer-shaped sills in analogue experiments. In *Structure and emplacement of high-level magmatic systems* (pp. 109–120). Geological Society, London.

Canet, C., Hernández-Cruz, B., Jiménez-Franco, A., Pi, T., Peláez, B., Villanueva-Estrada, R. E., ... Salinas, S. (2015). Combining ammonium mapping and short-wave infrared (SWIR) reflectance spectroscopy to constrain a model of hydrothermal alteration for the Acoculco geothermal zone, Eastern Mexico. *Geothermics*, *53*(July), 154–165. doi: 10.1016/j.geothermics.2014.05.012

Carrara, P., Ambati, M., Alessi, R., & Lorenzis, L. D. (2019). A framework to model the fatigue behavior of brittle materials based on a variational phase-field approach. *Computer Methods in Applied Mechanics and Engineering*, 112731. Retrieved from `http://www.sciencedirect.com/science/article/pii/S0045782519306218` doi: https://doi.org/10.1016/j.cma.2019.112731

Choo, J., & Sun, W. C. (2018). Cracking and damage from crystallization in pores: Coupled chemo-hydro-mechanics and phase-field modeling. *Computer Methods in Applied Mechanics and Engineering*, *335*(March), 347–379. doi:

10.1016/j.cma.2018.01.044

Chukwudozie, C., Bourdin, B., & Yoshioka, K. (2019). A variational phase-field model for hydraulic fracturing in porous media. *Computer Methods in Applied Mechanics and Engineering*, *347*, 957–982. Retrieved from https://doi.org/10.1016/j.cma.2018.12.037 doi: 10.1016/j.cma.2018.12.037

Chukwudozie, C., Bourdin, B., Yoshioka, K., Buchmann, T., & Connolly, P. (2013). A new modeling approach to natural fracturing process. *47th US Rock Mechanics / Geomechanics Symposium 2013*, *4*, 2663–2672.

Davies, R., Foulger, G., Bindley, A., & Styles, P. (2013). Induced seismicity and hydraulic fracturing for the recovery of hydrocarbons. *Marine and petroleum geology*, *45*, 171–185.

Del Piero, G. (1989). Constitutive equation and compatibility of the external loads for linear elastic masonry-like materials. *Meccanica*, *24*(3), 150–162. doi: 10.1007/BF01559418

Detournay, E. (2016). Mechanics of Hydraulic Fractures. *Annual Review of Fluid Mechanics*, *48*(1), 311–339. doi: 10.1146/annurev-fluid-010814-014736

Detournay, E., & Cheng, A. H. D. (1993). Fundamentals of poroelasticity. *Comprehensive rock engineering. Vol. 2*, *II*, 113–171. doi: 10.1017/cbo9781139051132.003

Economides, M. J., & Nolte, K. G. (1989). *Reservoir Stimulation* (No. Third Edition). Wiley. doi: 10.15713/ins.mmj.3

Ehlers, W., & Luo, C. (2017). A phase-field approach embedded in the Theory of Porous Media for the description of dynamic hydraulic fracturing. *Comput. Methods Appl. Mech. Engrg.*, *315*, 348–368. Retrieved from http://dx.doi.org/10.1016/j.cma.2016.10.045 doi: 10.1016/j.cma.2016.10.045

Elders, W. A., Fridhleifsson, G. Ó., & Albertsson, A. (2014). Drilling into magma and the implications of the Iceland Deep Drilling Project (IDDP) for high-temperature geothermal systems worldwide. *Geothermics*, *49*, 111–118.

Ellsworth, W. L., Giardini, D., Townend, J., Ge, S., & Shimamoto, T. (2019). Triggering of the Pohang, Korea, Earthquake (M w 5.5) by Enhanced Geothermal System Stimulation. *Seismological Research Letters*, *90*(5), 1844–1858.

Fischer, A. G., & Marigo, J.-J. (2019). Gradient damage models applied to dynamic fragmentation of brittle materials. *International Journal of Fracture*. Retrieved from https://doi.org/10.1007/s10704-019-00356-y doi: 10.1007/s10704-019-00356-y

Fox, D. B., Sutter, D., Beckers, K. F., Lukawski, M. Z., Koch, D. L., Anderson, B. J., & Tester, J. W. (2013). Sustainable heat farming: Modeling extraction and recovery in discretely fractured geothermal reservoirs. *Geothermics*, *46*, 42–54. Retrieved from http://dx.doi.org/10.1016/j.geothermics.2012.09.001 doi: 10.1016/j.geothermics.2012.09.001

Francfort, G. A., & Marigo, J.-J. (1998). Revisiting brittle fracture as an energy minimization problem. *J. Mech. and Phys. of Solids*, *46*(8), 1319–1342.

Franklin, J. A., Zongqi, S., Atkinson, B. K., Meredith, P. G., Rummel, F., Muller, W., ... Bobrov, G. F. (1988). ISRM SUGGESTED METHODS FOR DETERMINING THE FRACTURE TOUGHNESS OF ROCK. *International Journal of Rock Mechanics and Mining Sciences & Geomechanics Abstracts*, *25*(2), 71–96. Retrieved from http://linkinghub.elsevier.com/retrieve/pii/S0148906296000150 doi: 10.1016/S0148-9062(96)00015-0

Freddi, F., & Royer-Carfagni, G. (2011). Variational fracture mechanics to model compressive splitting of masonry-like materials. *Annals of Solid and Structural Mechanics*, *2*(2-4), 57–67. doi: 10.1007/s12356-011-0018-4

Fu, P., Settgast, R. R., Hao, Y., Morris, J. P., & Ryerson, F. J. (2017). The Influence of Hydraulic Fracturing on Carbon Storage Performance. *Journal of Geophysical Research: Solid Earth*, *122*(12), 9931–9949. doi: 10.1002/2017JB014942

667 Gao, H., & Rice, J. R. (1987). Somewhat circular tensile cracks. *International Jour-*
668 *nal of Fracture*, 155–174.
669 Garagash, D., & Detournay, E. (2000). The tip region of a fluid-driven fracture in an
670 elastic medium. *J. Appl. Mech.*, *67*(1), 183–192.
671 Garagash, D. I., Detournay, E., & Adachi, J. I. (2011). Multiscale tip asymptotics in
672 hydraulic fracture with leak-off. *Journal of Fluid Mechanics*, *669*, 260–297.
673 Garagash, D. I., & Germanovich, L. N. (2012). Nucleation and arrest of dy-
674 namic slip on a pressurized fault. *Journal of Geophysical Research: Solid Earth*,
675 *117*(B10).
676 Geertsma, J., & De Klerk, F. (1969). Rapid Method of Predicting Width and Extent
677 of Hydraulically Induced Fractures. *J Petroleum Technology*, *21*(12), 1571–1581.
678 doi: 10.2118/2458-pa
679 Griffith, A. A. (1921). The Phenomena of Rupture and Flow in Solids. *Philo-*
680 *sophical transactions of the royal society of london. Series A, containing papers*
681 *of a mathematical or physical character*, *221*(1921), 163–198. Retrieved from
682 `https://www.jstor.org/stable/91192`
683 Guo, H., Aziz, N. I., & Schmidt, L. C. (1993). Rock fracture-toughness determina-
684 tion by the Brazilian test. *Engineering Geology*, *33*(3), 177–188. doi: 10.1016/0013
685 -7952(93)90056-I
686 Gupta, P., & Duarte, C. A. (2016). Coupled formulation and algorithms for the
687 simulation of non-planar three-dimensional hydraulic fractures using the general-
688 ized finite element method. *International Journal for Numerical and Analytical*
689 *Methods in Geomechanics*, *40*(10), 1402–1437. doi: 10.1002/nag.2485
690 Hansen-Dörr, A. C., de Borst, R., Hennig, P., & Kästner, M. (2019). Phase-
691 field modelling of interface failure in brittle materials. *Computer Meth-*
692 *ods in Applied Mechanics and Engineering*, *346*, 25–42. Retrieved from
693 `http://www.sciencedirect.com/science/article/pii/S0045782518305772`
694 doi: https://doi.org/10.1016/j.cma.2018.11.020
695 Heidbach, O., Rajabi, M., Reiter, K., Ziegler, M., & Team WSM. (2016). World
696 Stress Map Database Release 2016. *GFZ Data Services*. Retrieved from `http://`
697 `doi.org/10.5880/WSM.2016.001`
698 Heider, Y., & Markert, B. (2017). A phase-field modeling approach of hydraulic frac-
699 ture in saturated porous media. *Mechanics Research Communications*, *80*, 38–46.
700 Retrieved from `http://dx.doi.org/10.1016/j.mechrescom.2016.07.002` doi:
701 10.1016/j.mechrescom.2016.07.002
702 Hofacker, M., & Miehe, C. (2012). Continuum phase field modeling of dynamic frac-
703 ture: Variational principles and staggered FE implementation. *International Jour-*
704 *nal of Fracture*, *178*(1-2), 113–129. doi: 10.1007/s10704-012-9753-8
705 Irwin, G. R. (1957). Analysis of Stresses and Strains Near the End of a Crack
706 Traversing a Plate. *Journal of Applied Mechanics*, *24*, 361–364.
707 Jeffrey, R. G., Bunger, A. P., Lecampion, B., Zhang, X., Chen, Z. R., Van As, A., ...
708 Mainguy, M. (2009). Measuring hydraulic fracture growth in naturally fractured
709 rock. *Proceedings - SPE Annual Technical Conference and Exhibition*, *6*(January),
710 3750–3768. doi: 10.2118/124919-ms
711 Jeffrey, R. G., Weber, C. R., Vlahovic, W., & Enever, J. R. (1994). Hydraulic frac-
712 turing experiments in the great northern coal seam. *SPE - Asia Pacific Oil & Gas*
713 *Conference*, 361–371. doi: 10.2523/28779-ms
714 Karypis, G., & Kumar, V. (1998). A fast and high quality multilevel scheme for par-
715 titioning irregular graphs. *SIAM Journal of Scientific Computing*, *20*(1), 359–392.
716 doi: 10.1137/S1064827595287997
717 Kolditz, O., Bauer, S., Bilke, L., Böttcher, N., Delfs, J. O., Fischer, T., ... Zehner,
718 B. (2012). OpenGeoSys: An open-source initiative for numerical simulation of
719 thermo-hydro-mechanical/chemical (THM/C) processes in porous media. *Environ-*
720 *mental Earth Sciences*, *67*(2), 589–599. doi: 10.1007/s12665-012-1546-x

Kuhn, C., Noll, T., & Müller, R. (2016). On phase field modeling of ductile fracture. *GAMM Mitteilungen*, *39*(1), 35–54. doi: 10.1002/gamm.201610003

Lecampion, B., Bunger, A., & Zhang, X. (2018). Numerical methods for hydraulic fracture propagation: a review of recent trends. *Journal of natural gas science and engineering*, *49*, 66–83.

Lee, S., Wheeler, M. F., & Wick, T. (2017). Iterative coupling of flow, geomechanics and adaptive phase-field fracture including level-set crack width approaches. *Journal of Computational and Applied Mathematics*, *314*, 40–60. Retrieved from `http://dx.doi.org/10.1016/j.cam.2016.10.022` doi: 10.1016/j.cam.2016.10.022

Legarth, B. A., & Saadat, A. (2005). Energy Consumption for Geothermal Wells. *Database*(April), 24–29.

Lepillier, B., Bruna, P.-O., Bruhn, D., Bastesen, E., Daniilidis, A., Garcia, Ó., ... Wheeler, W. (2020). From outcrop scanlines to discrete fracture networks, an integrative workflow. *Journal of Structural Geology*, *133*(January), 103992. Retrieved from `http://www.sciencedirect.com/science/article/pii/S0191814119303050` doi: https://doi.org/10.1016/j.jsg.2020.103992

Lepillier, B., Daniilidis, A., Gholizadeh, N., Bruna, P.-o., Juliane, K., & Bruhn, D. (2019). A fracture flow permeability and stress dependency simulation applied to multi-reservoirs , multi-production scenarios analysis. *Geothermal Energy*. Retrieved from `https://rdcu.be/bPyIc` doi: https://doi.org/10.1186/s40517-019-0141-8

Li, T., Marigo, J.-J., Guilbaud, D., & Potapov, S. (2016). Gradient damage modeling of brittle fracture in an explicit dynamic context. *International Journal for Numerical Methods in Engineering*, *00*(March), 1–25. doi: 10.1002/nme

Liotta, D., Bastesen, E., Bianco, C., Brogi, A., Caggianelli, A., Garduño-Monroy, V.-H., ... Zucchi, M. (2020). Analogue Geothermal Systems In Mexico : Insights Into The Deep Part Of Los Humeros Geothermal Field From The Las Minas Mining Area (Eastern Mexico). *Proceedings World Geothermal Congress 2020*, 1–9.

Lopez-Comino, J. A., Cesca, S., Kriegerowski, M., Heimann, S., Dahm, T., Mirek, J., & Lasocki, S. (2017). Monitoring performance using synthetic data for induced microseismicity by hydrofracking at the Wysin site (Poland). *Geophysical Journal International*, 42–55.

López-Hernández, A., García-Estrada, G., Aguirre-Díaz, G., González-Partida, E., Palma-Guzmán, H., & Quijano-León, J. L. (2009). Hydrothermal activity in the Tulancingo-Acoculco Caldera Complex, central Mexico: Exploratory studies. *Geothermics*, *38*(3), 279–293. doi: 10.1016/j.geothermics.2009.05.001

Lu, R., Nagel, T., Shao, H., Kolditz, O., & Shao, H. (2018). Modeling of Dissolution-Induced Permeability Evolution of a Granite Fracture Under Crustal Conditions. *Journal of Geophysical Research: Solid Earth*, *123*(7), 5609–5627.

McClure, M. W., & Horne, R. N. (2014). An investigation of stimulation mechanisms in Enhanced Geothermal Systems. *International Journal of Rock Mechanics and Mining Sciences*, *72*(November), 242–260. Retrieved from `http://dx.doi.org/10.1016/j.ijrmms.2014.07.011` doi: 10.1016/j.ijrmms.2014.07.011

McClure Mark, W., Mohsen, B., Sogo, S., & Jian, H. (2015). Fully coupled hydromechanical simulation of hydraulic fracturing in 3D discrete-fracture networks. *SPE Journal*, *21*(4), 1302–1320. doi: 10.2118/173354-ms

Miehe, C., Hofacker, M., Schänzel, L. M., & Aldakheel, F. (2015). Phase field modeling of fracture in multi-physics problems. Part II. Coupled brittle-to-ductile failure criteria and crack propagation in thermo-elastic-plastic solids. *Computer Methods in Applied Mechanics and Engineering*, *294*, 486–522. doi: 10.1016/j.cma.2014.11.017

Miehe, C., Mauthe, S., & Teichtmeister, S. (2015). Minimization principles for the

coupled problem of Darcy-Biot-type fluid transport in porous media linked to phase field modeling of fracture. *Journal of the Mechanics and Physics of Solids*, *82*, 186–217. Retrieved from http://dx.doi.org/10.1016/j.jmps.2015.04.006 doi: 10.1016/j.jmps.2015.04.006

Miehe, C., Welschinger, F., & Hofacker, M. (2010). Thermodynamically consistent phase-field models of fracture: Variational principles and multi-field FE implementations. *International Journal for Numerical Methods in Engineering*, *83*(10), 1273–1311. Retrieved from http://dx.doi.org/10.1002/nme.2861 doi: 10.1002/nme.2861

Mikelić, A., Wheeler, M. F., & Wick, T. (2015). A Phase-Field method for propagating fluid-filled fractures coupled to a surrounding porous medium. *Multiscale Modeling & Simulation*, *48*(1), 162–186.

Milanese, E., Rizzato, P., Pesavento, F., Secchi, S., & Schrefler, B. A. (2016). An explanation for the intermittent crack tip advancement and pressure fluctuations in hydraulic fracturing. *Hydraul Fract J*, *3*(2), 30–43.

Moës, N., Dolbow, J., & Belytschko, T. (1999). A finite element method for crack growth without remeshing. *International Journal for Numerical Methods in Engineering*, *46*(1), 131–150. doi: 10.1002/(SICI)1097-0207(19990910)46:1⟨131::AID-NME726⟩3.0.CO;2-J

Nordgren, R. P. (1972). Propagation of a Vertical Hydraulic Fracture. *Society of Petroleum Engineers Journal*, *12*(04), 306–314. doi: 10.2118/3009-pa

Perkins, T. K., & Kern, L. R. (1961). Widths of Hydraulic Fractures. *Journal of Petroleum Technology*, *13*(09), 937–949. doi: 10.2118/89-pa

Renshaw, C. E., & Pollard, D. D. (1995). An experimentally verified criterion for propagation across unbounded frictional interfaces in brittle, linear elastic materials. *International Journal of Rock Mechanics and Mining Sciences and*, *32*(3), 237–249. doi: 10.1016/0148-9062(94)00037-4

Santillán, D., Juanes, R., & Cueto-Felgueroso, L. (2017). Phase field model of fluid-driven fracture in elastic media: Immersed-fracture formulation and validation with analytical solutions. *J Geophus. Res.-Sol Ea.*. doi: 10.1002/2016JB013572

Savitski, A. A., & Detournay, E. (2002). Propagation of a penny-shaped fluid-driven fracture in an impermeable rock: asymptotic solutions. *International journal of solids and structures*, *39*(26), 6311–6337.

Schlüter, A., Willenbücher, A., Kuhn, C., & Müller, R. (2014). Phase field approximation of dynamic brittle fracture. *Computational Mechanics*, *54*(5), 1141–1161. doi: 10.1007/s00466-014-1045-x

Schultz, R., Stern, V., Novakovic, M., Atkinson, G., & Gu, Y. J. (2015). Hydraulic fracturing and the Crooked Lake Sequences: Insights gleaned from regional seismic networks. *Geophysical Research Letters*, *42*(8), 2750–2758.

Scott, S. W., & Driesner, T. (2018). Permeability changes resulting from quartz precipitation and dissolution around upper crustal intrusions. *Geofluids*, *2018*.

Seiler, M., Hantschke, P., Brosius, A., & Kästner, M. (2018). A numerically efficient phase-field model for fatigue fracture - 1D analysis. *Pamm*, *18*(1), e201800207. doi: 10.1002/pamm.201800207

Shiozawa, S., Lee, S., & Wheeler, M. F. (2019). The effect of stress boundary conditions on fluid-driven fracture propagation in porous media using a phase-field modeling approach. *International Journal for Numerical and Analytical Methods in Geomechanics*(February 2018), 1–25. doi: 10.1002/nag.2899

Singurindy, O., & Berkowitz, B. (2005). The role of fractures on coupled dissolution and precipitation patterns in carbonate rocks. *Advances in water resources*, *28*(5), 507–521.

Tanne, E. (2017). *Thèse de doctorat de l ' université Paris-Saclay* (Unpublished doctoral dissertation).

Tanné, E., Li, T., Bourdin, B., Marigo, J.-J., & Maurini, C. (2018). Crack nucle-

ation in variational phase-field models of brittle fracture. *J. Mech. Phys. Solids*, *110*, 80–99. doi: 10.1016/j.jmps.2017.09.006

Tsai, V. C., & Rice, J. R. (2010). A model for turbulent hydraulic fracture and application to crack propagation at glacier beds. *Journal of Geophysical Research: Earth Surface*, *115*(F3).

Wang, H. Y. (2019). Hydraulic fracture propagation in naturally fractured reservoirs: Complex fracture or fracture networks. *Journal of Natural Gas Science and Engineering*, *68*(June), 102911. Retrieved from `https://doi.org/10.1016/j.jngse.2019.102911` doi: 10.1016/j.jngse.2019.102911

Warpinski, N. R., & Teufel, L. W. (1987). Influence of Geologic Discontinuities on Hydraulic Fracture Propagation (includes associated papers 17011 and 17074). *Journal of Petroleum Technology*, *39*(02), 209–220. doi: 10.2118/13224-pa

Watanabe, N., Saito, K., Okamoto, A., Nakamura, K., Ishibashi, T., Saishu, H., ... Tsuchiya, N. (2020). Stabilizing and enhancing permeability for sustainable and profitable energy extraction from superhot geothermal environments. *Applied Energy*, *260*, 114306.

Weng, X. (2014). Modeling of complex hydraulic fractures in naturally fractured formation. *Journal of Unconventional Oil and Gas Resources*, *9*, 114–135. Retrieved from `http://dx.doi.org/10.1016/j.juogr.2014.07.001` doi: 10.1016/j.juogr.2014.07.001

Weng, X., Kresse, O., Cohen, C., Wu, R., & Gu, H. (2011). Modeling of hydraulic fracture network propagation in a naturally fractured formation. *Society of Petroleum Engineers - SPE Hydraulic Fracturing Technology Conference 2011*, *i*, 298–315. doi: 10.2118/140253-ms

Weydt, L., Bär, K., Colombero, C., Comina, C., Deb, P., Lepillier, B., ... Sass, I. (2018). Outcrop analogue study to determine reservoir properties of the Los Humeros and Acoculco geothermal fields, Mexico. *Geophysical Research Abstracts EGU General Assembly*, *20*(727550), 2018–7228. doi: 10.5194/adgeo-45-281-2018

Wheeler, M. F., Wick, T., & Wollner, W. (2014). An augmented-Lagrangian method for the phase-field approach for pressurized fractures. *Computer Methods in Applied Mechanics and Engineering*, *271*, 69–85. Retrieved from `http://dx.doi.org/10.1016/j.cma.2013.12.005` doi: 10.1016/j.cma.2013.12.005

Wilson, Z., & Landis, C. (2016). Phase-field modeling of hydraulic fracture. *J. Mech. Phys. Solids*, *96*, 264–290. Retrieved from `http://dx.doi.org/10.1016/j.jmps.2016.07.019` doi: 10.1016/j.jmps.2016.07.019

Xia, L., Yvonnet, J., & Ghabezloo, S. (2017). Phase field modeling of hydraulic fracturing with interfacial damage in highly heterogeneous fluid-saturated porous media. *Engineering Fracture Mechanics*, *186*(October), 158–180. doi: 10.1016/j.engfracmech.2017.10.005

Yazid, A., Abdelkader, N., & Abdelmadjid, H. (2009). A state-of-the-art review of the X-FEM for computational fracture mechanics. *Applied Mathematical Modelling*, *33*(12), 4269–4282. doi: 10.1016/j.apm.2009.02.010

Yew, C. H., & Weng, X. (2015). Fracture propagation in a naturally fractured formation. *Mechanics of Hydraulic Fracturing*, *1*, 133–175. doi: 10.1016/b978-0-12-420003-6.00007-0

Yoshioka, K., & Bourdin, B. (2016). A variational hydraulic fracturing model coupled to a reservoir simulator. *International Journal of Rock Mechanics and Mining Sciences*, *88*, 137–150. Retrieved from `http://dx.doi.org/10.1016/j.ijrmms.2016.07.020` doi: 10.1016/j.ijrmms.2016.07.020

Yoshioka, K., Parisio, F., Naumov, D., Lu, R., Kolditz, O., & Nagel, T. (2019). Comparative verification of discrete and smeared numerical approaches for the simulation of hydraulic fracturing. *GEM - International Journal on Geomathematics*, *10*(1), 1–35. Retrieved from `https://doi.org/10.1007/s13137-019-0126-6` doi: 10.1007/s13137-019-0126-6

Zoback, M. D., Barton, C. A., Brudy, M., Castillo, D. A., Finkbeiner, T., Grollimund, B. R., ... Wiprut, D. J. (2003). Determination of stress orientation and magnitude in deep wells. *International Journal of Rock Mechanics and Mining Sciences*, *40*(7-8), 1049–1076. doi: 10.1016/j.ijrmms.2003.07.001

Figure 1.

Time Step = [initial]

HF approaching NF...

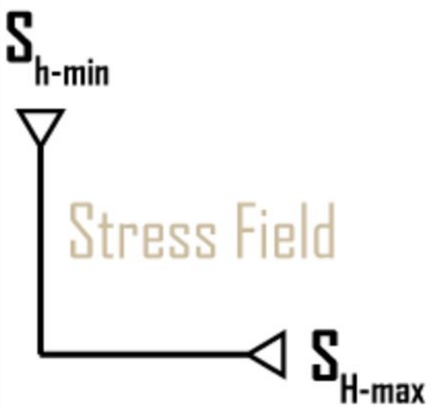

Time Step = [intermediate]

HF stopped

HF propagates in NF (=branching)

HF crosses

HF branches + crosses NF

HF crosses with offset

HF branches + crosses + with offset

Figure 2.

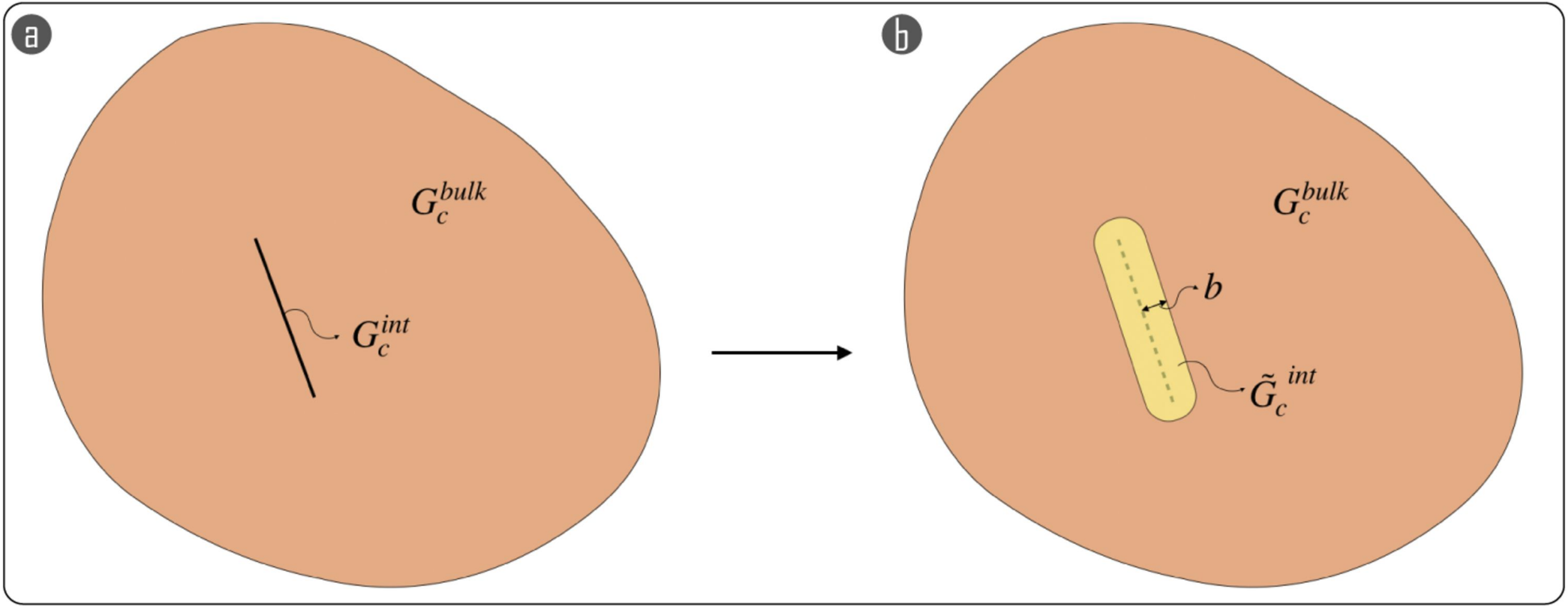
a
G_c^{bulk}
G_c^{int}
b
G_c^{bulk}
b
$\tilde{G}_c^{int}$

Figure 3.

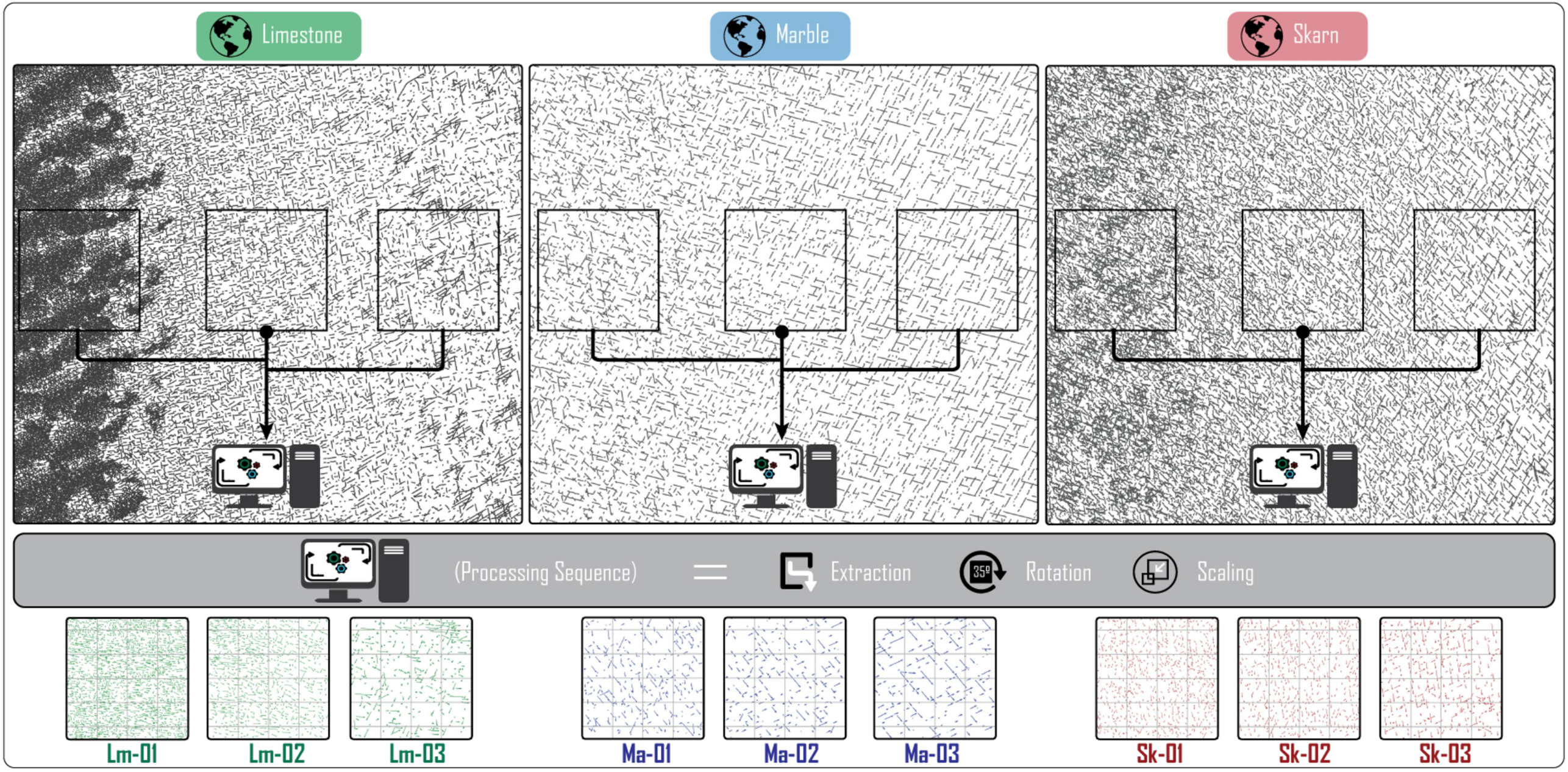
Limestone
Marble
Skarn
(Processing Sequence)
Extraction
Rotation
Scaling
Lm-01
Lm-02
Lm-03
Ma-01
Ma-02
Ma-03
Sk-01
Sk-02
Sk-03

Figure 4.

a Griffith's critical energy release rate (G_c)

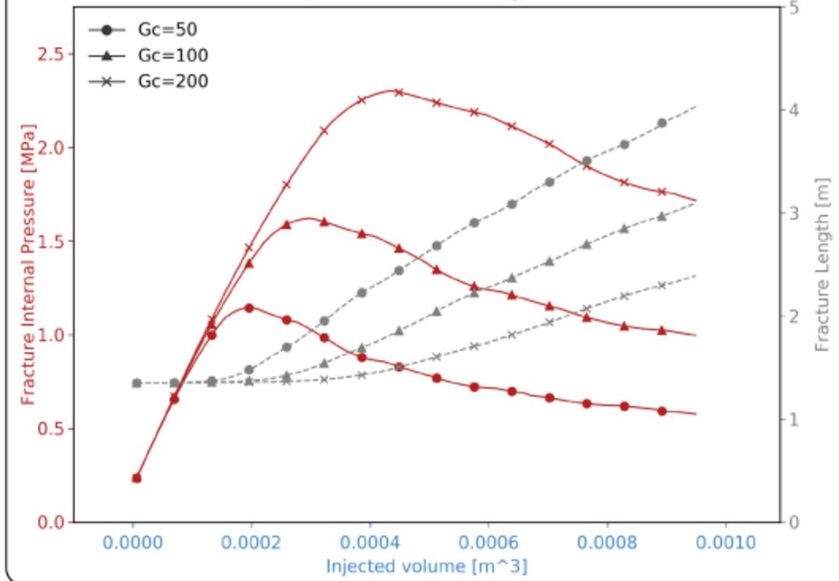

b Young's modulus (E)

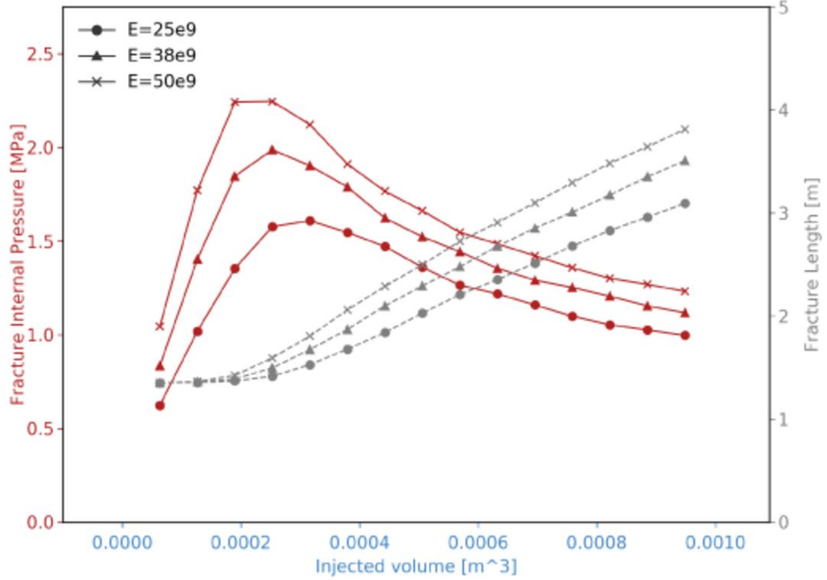

c Poisson's ratio (ν)

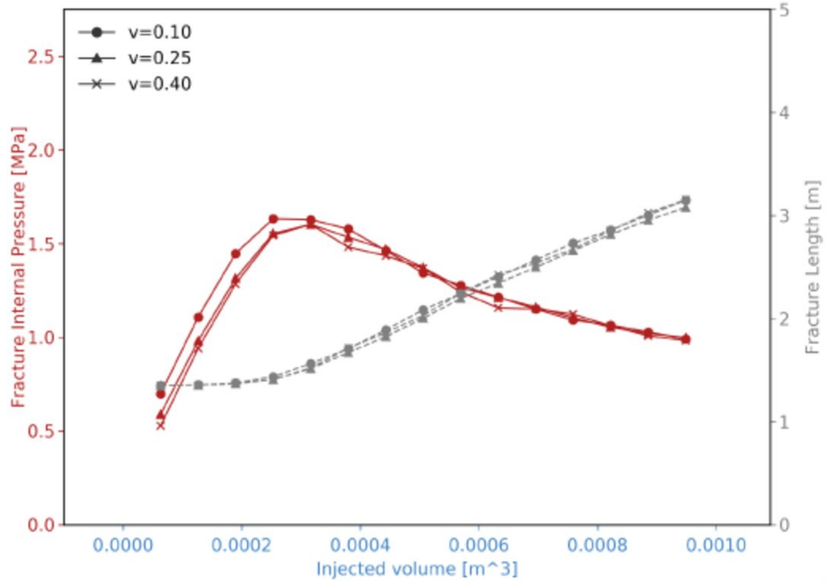

Figure 5.

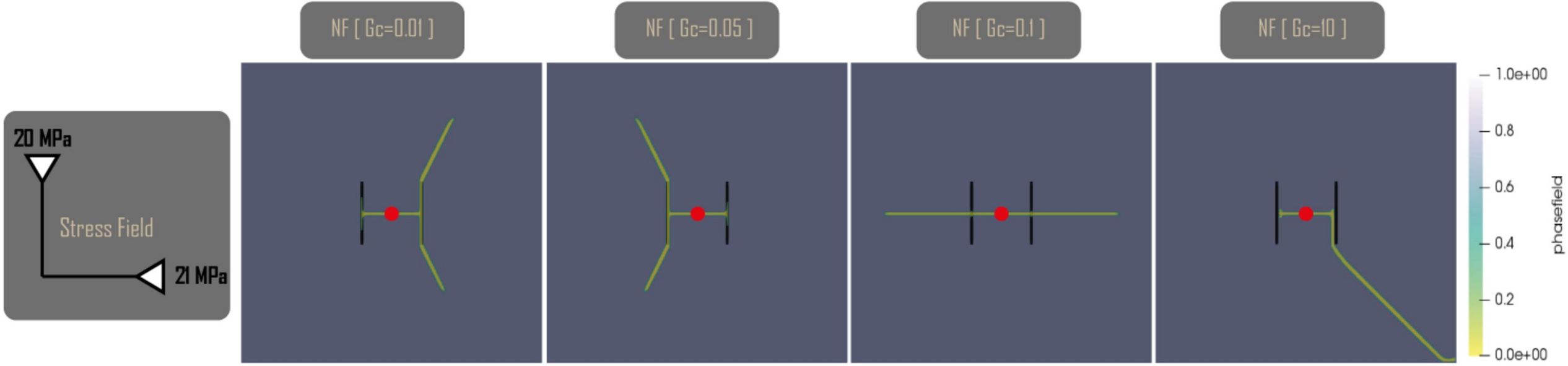
NF [Gc=0.01]
NF [Gc=0.05]
NF [Gc=0.1]
NF [Gc=10]
20 MPa
Stress Field
21 MPa
1.0e+00
0.8
0.6
0.4
0.2
0.0e+00
phasefield

Figure 6.

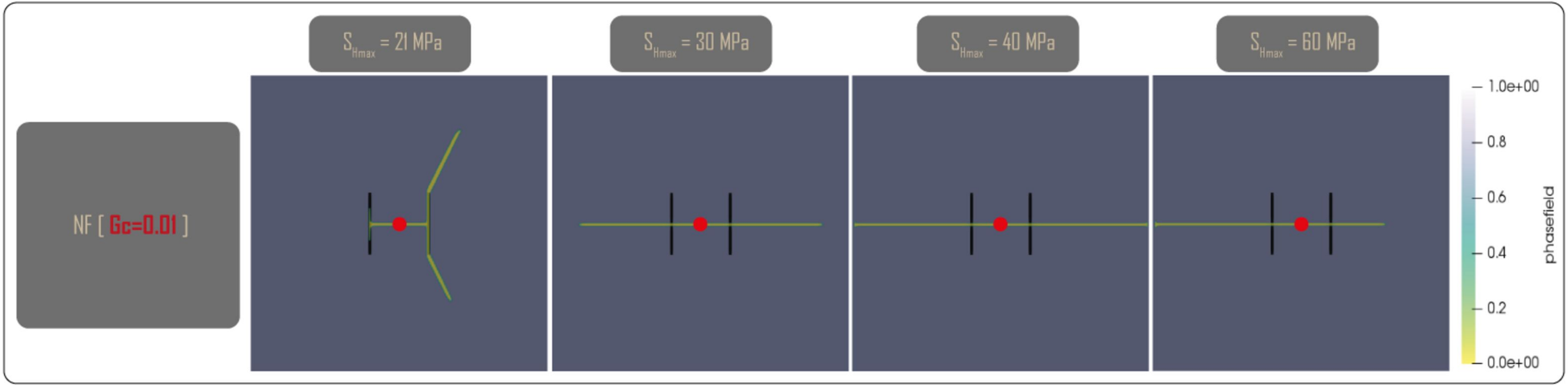
NF [Gc=0.01]
S_{Hmax} = 21 MPa
S_{Hmax} = 30 MPa
S_{Hmax} = 40 MPa
S_{Hmax} = 60 MPa
1.0e+00
0.8
0.6
0.4
0.2
0.0e+00
phasefield

Figure 7.

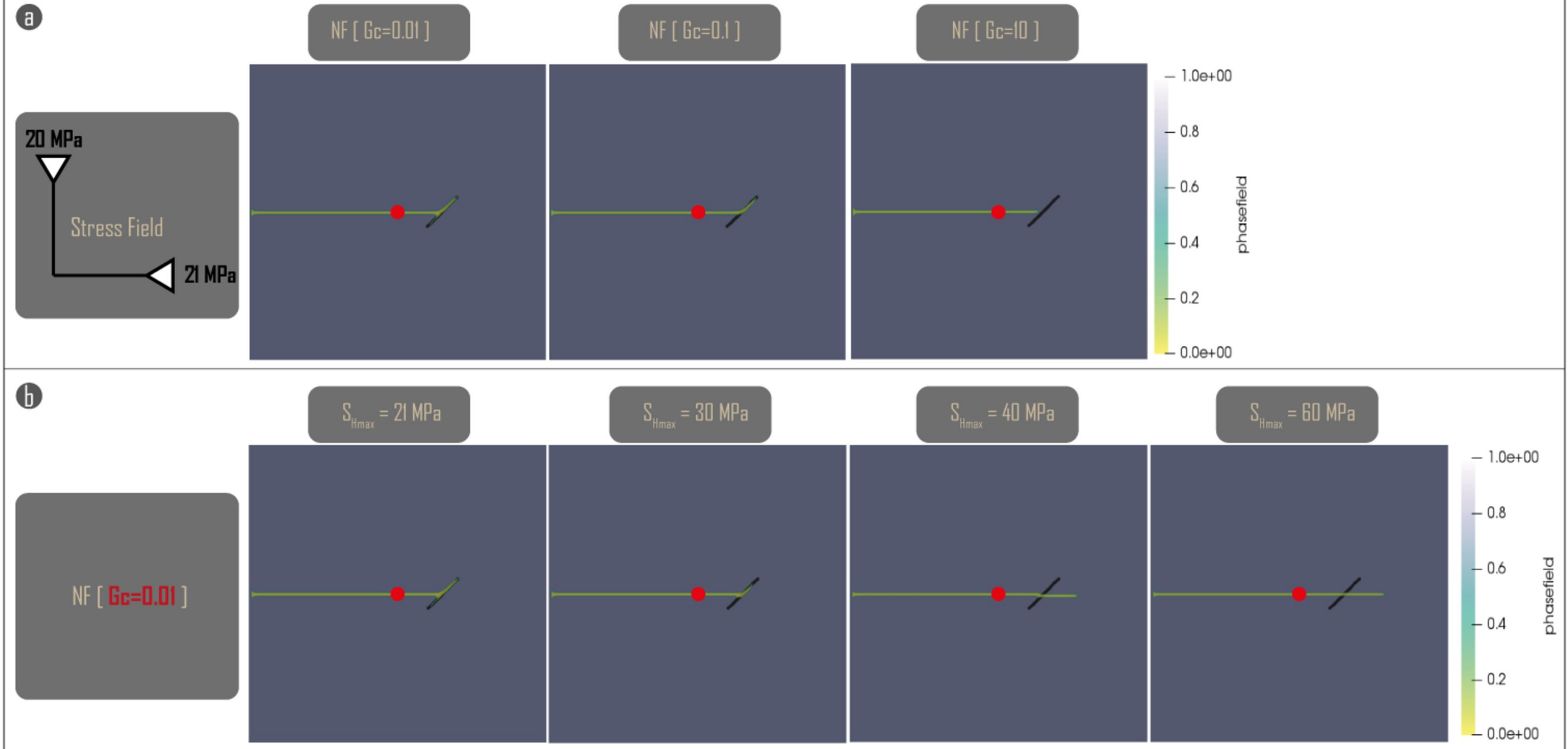
a
NF [Gc=0.01]
NF [Gc=0.1]
NF [Gc=10]
20 MPa
Stress Field
21 MPa
1.0e+00
0.8
0.6
0.4
0.2
0.0e+00
phasefield
b
NF [Gc=0.01]
S_Hmax = 21 MPa
S_Hmax = 30 MPa
S_Hmax = 40 MPa
S_Hmax = 60 MPa
1.0e+00
0.8
0.6
0.4
0.2
0.0e+00
phasefield

Figure 8.

HF propagation plot

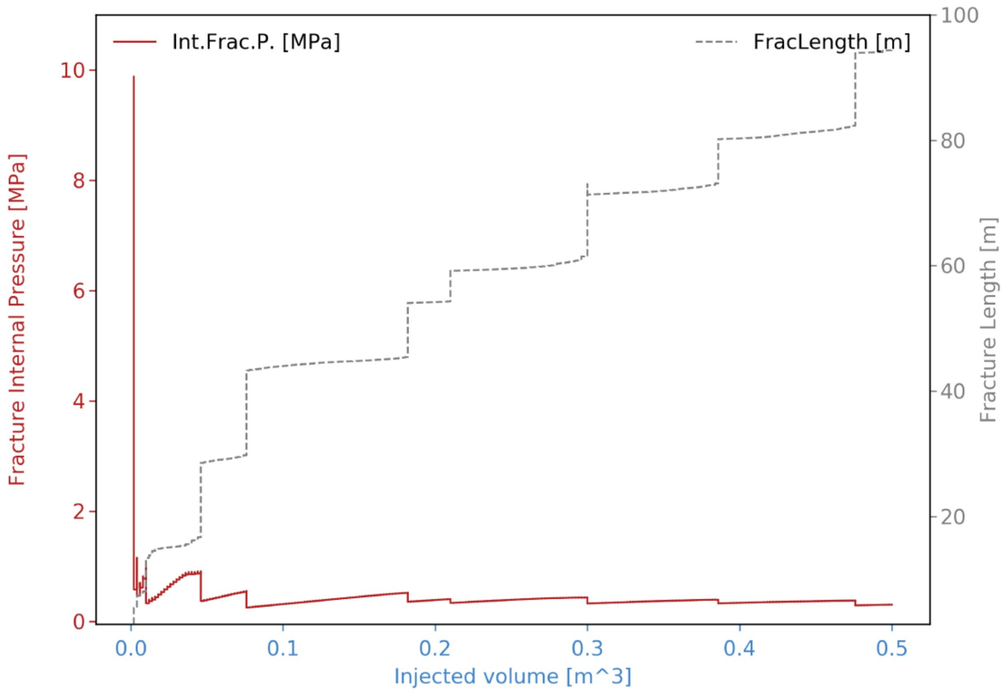

Ω + Γ Limestone: Lm01

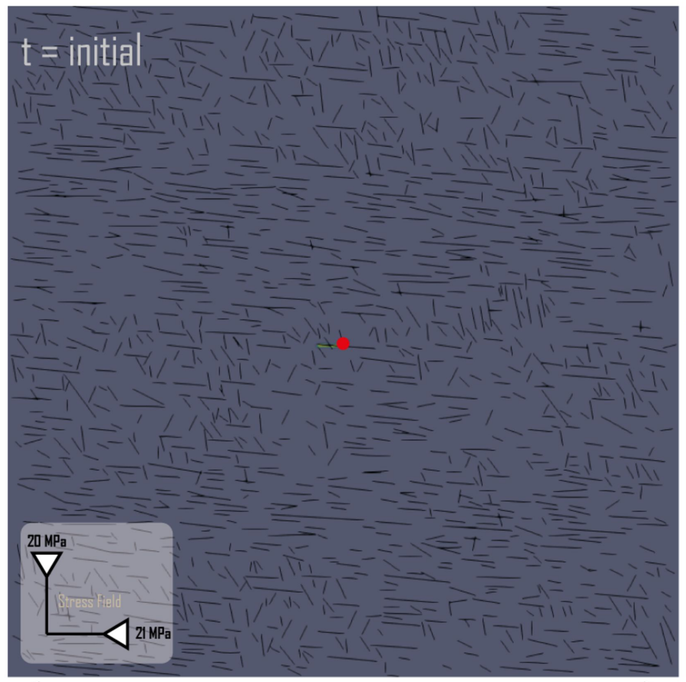

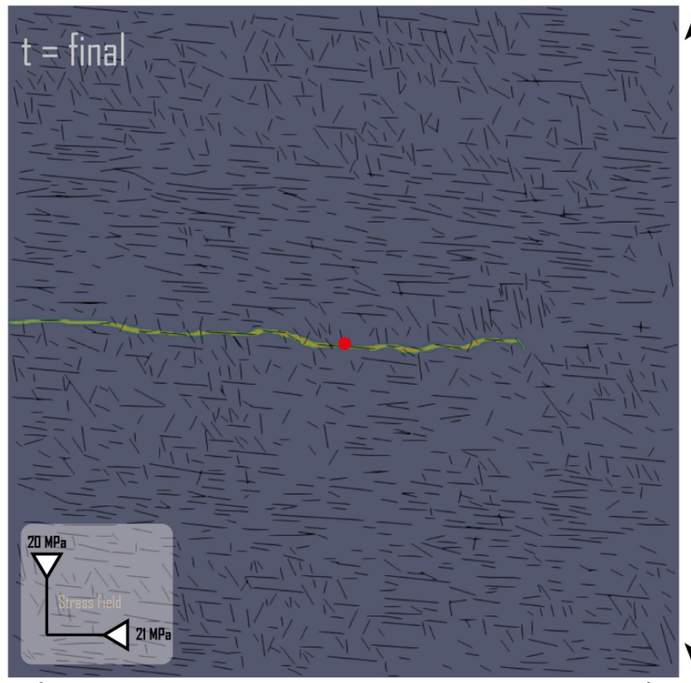

100m

100m

100m

Phase field

HF propagation plot

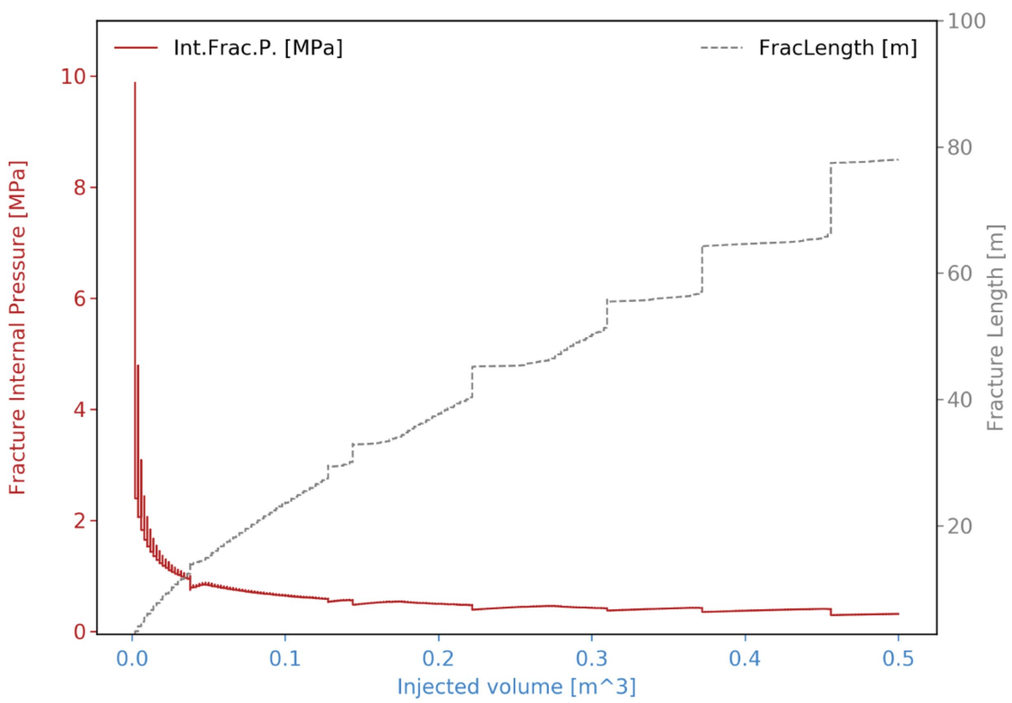

Ω + Γ Limestone: Lm02

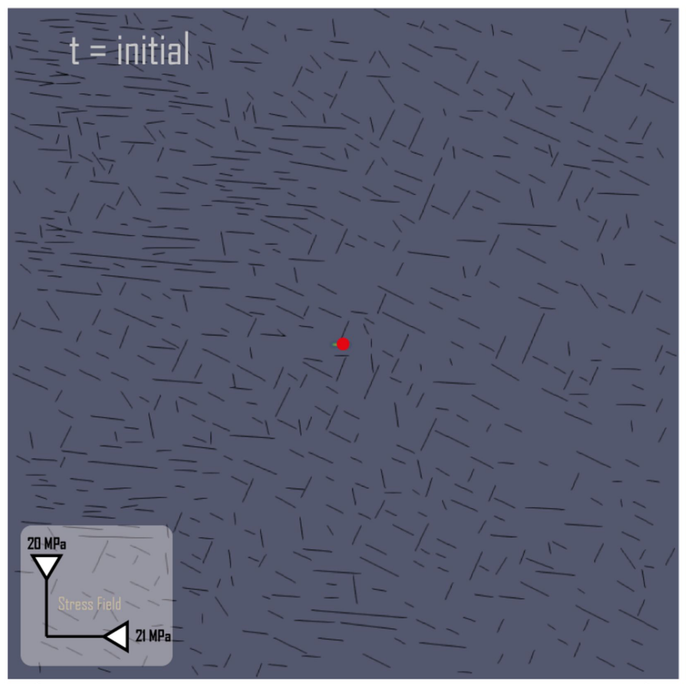

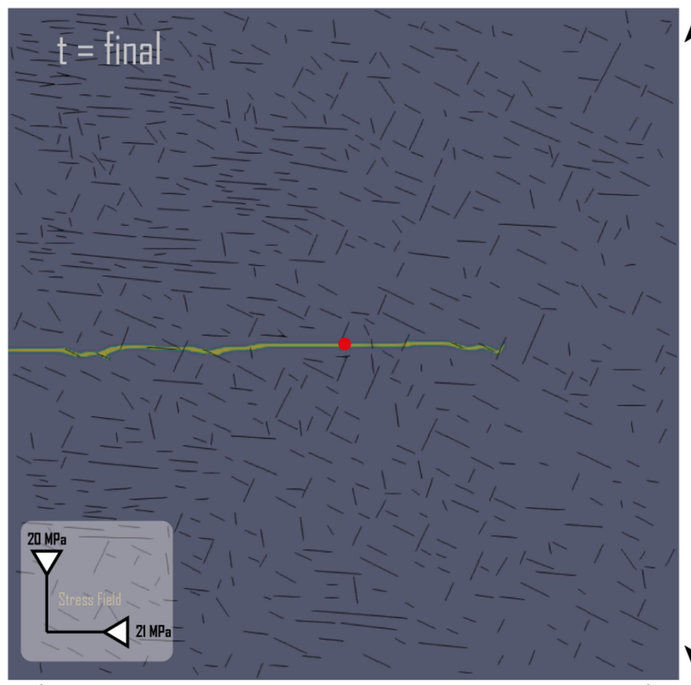

100m

100m

100m

Phase-field

HF propagation plot

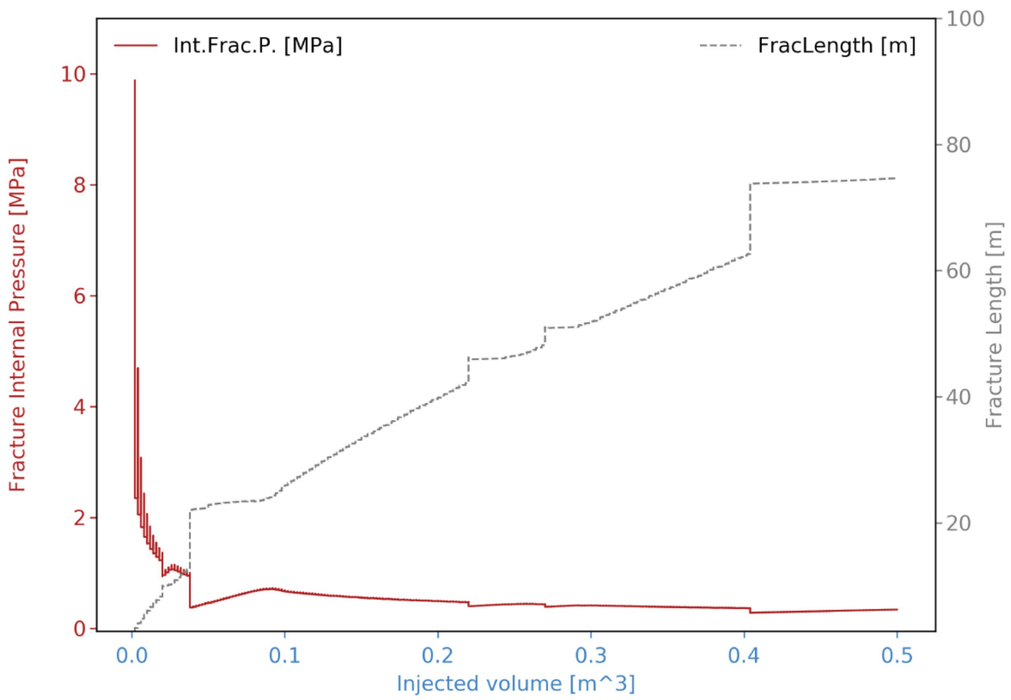

Ω + Γ Limestone: Lm03

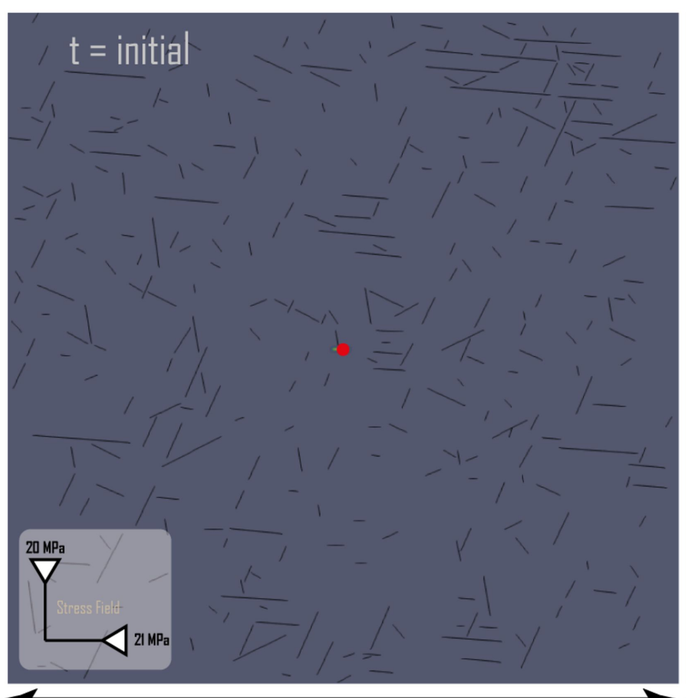

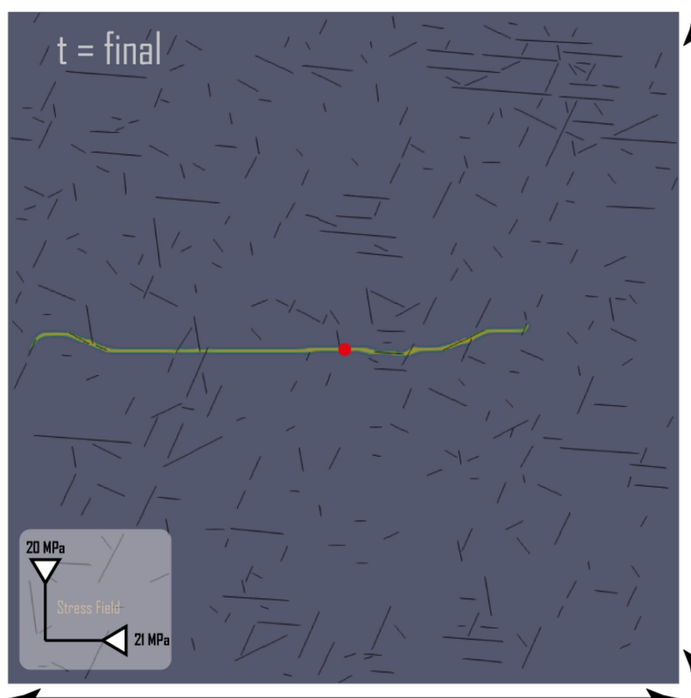

100m

100m

100m

Phase-field

Figure 9.

HF propagation plot

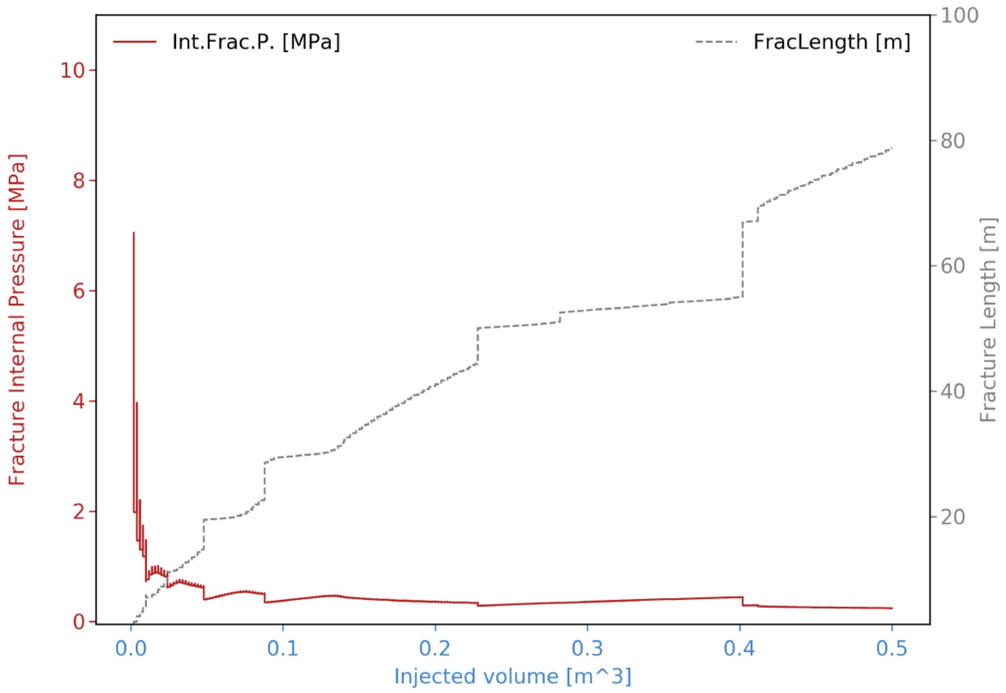

Ω + Γ Marble: Ma01

Phase field

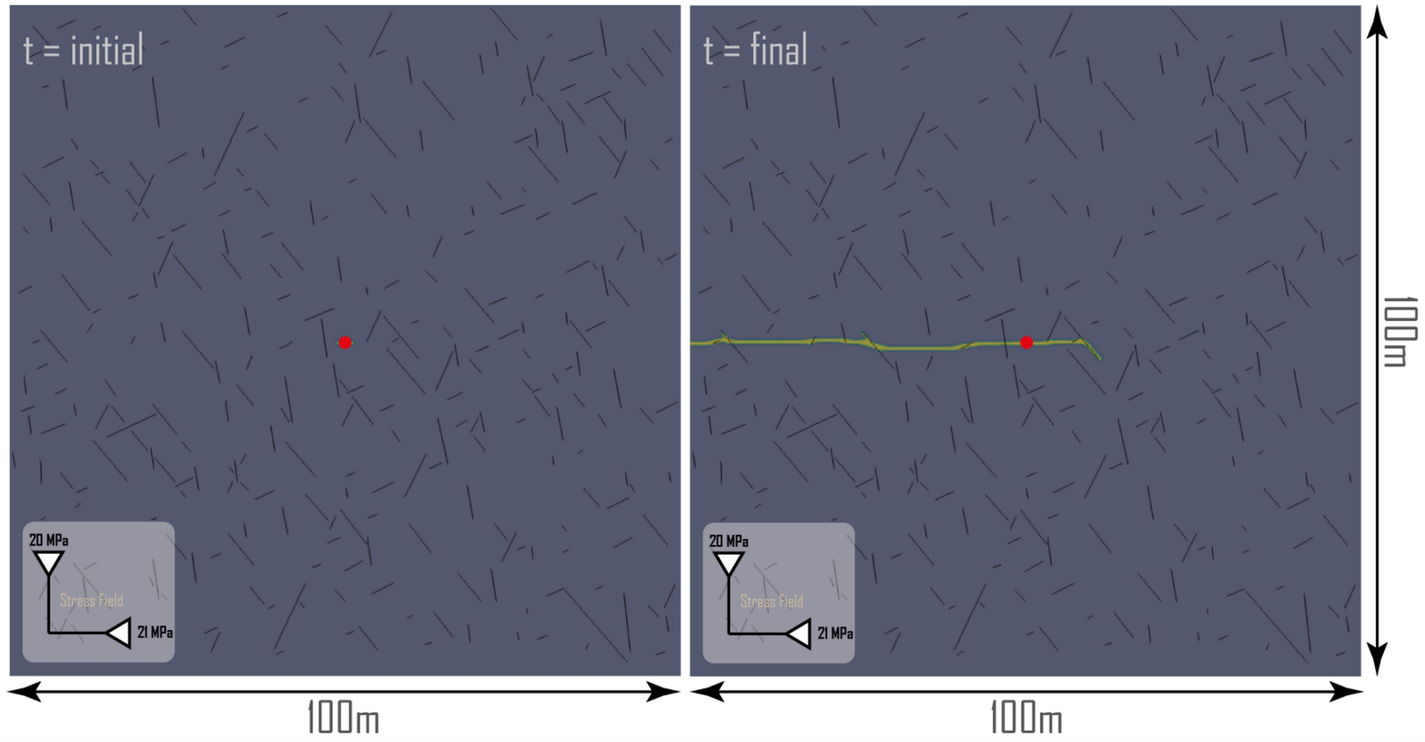

HF propagation plot

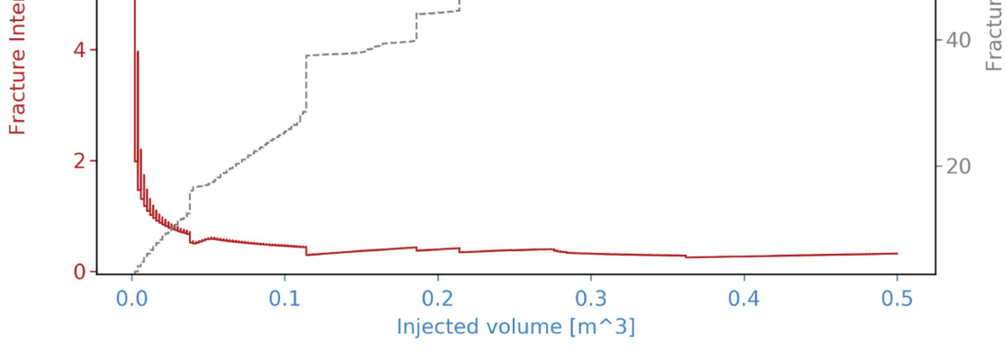

Ω + Γ Marble: Ma02

Phase-field

HF propagation plot

Ω + Γ Marble: Ma03

Phase-field

Figure 10.

HF propagation plot

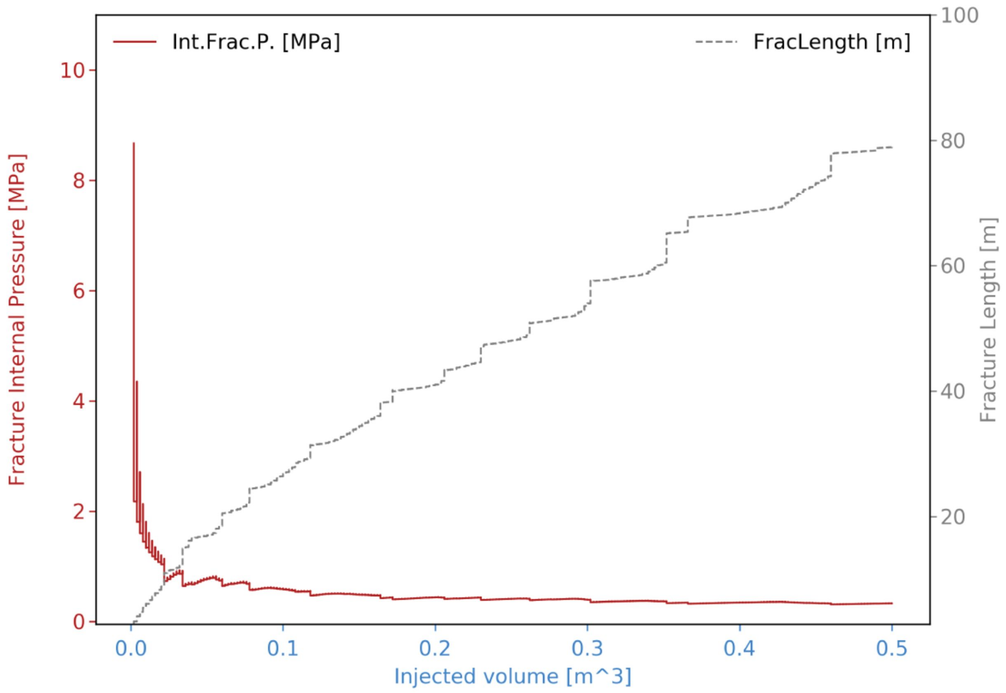

Ω + Γ Skarn: Sk01

Phase field

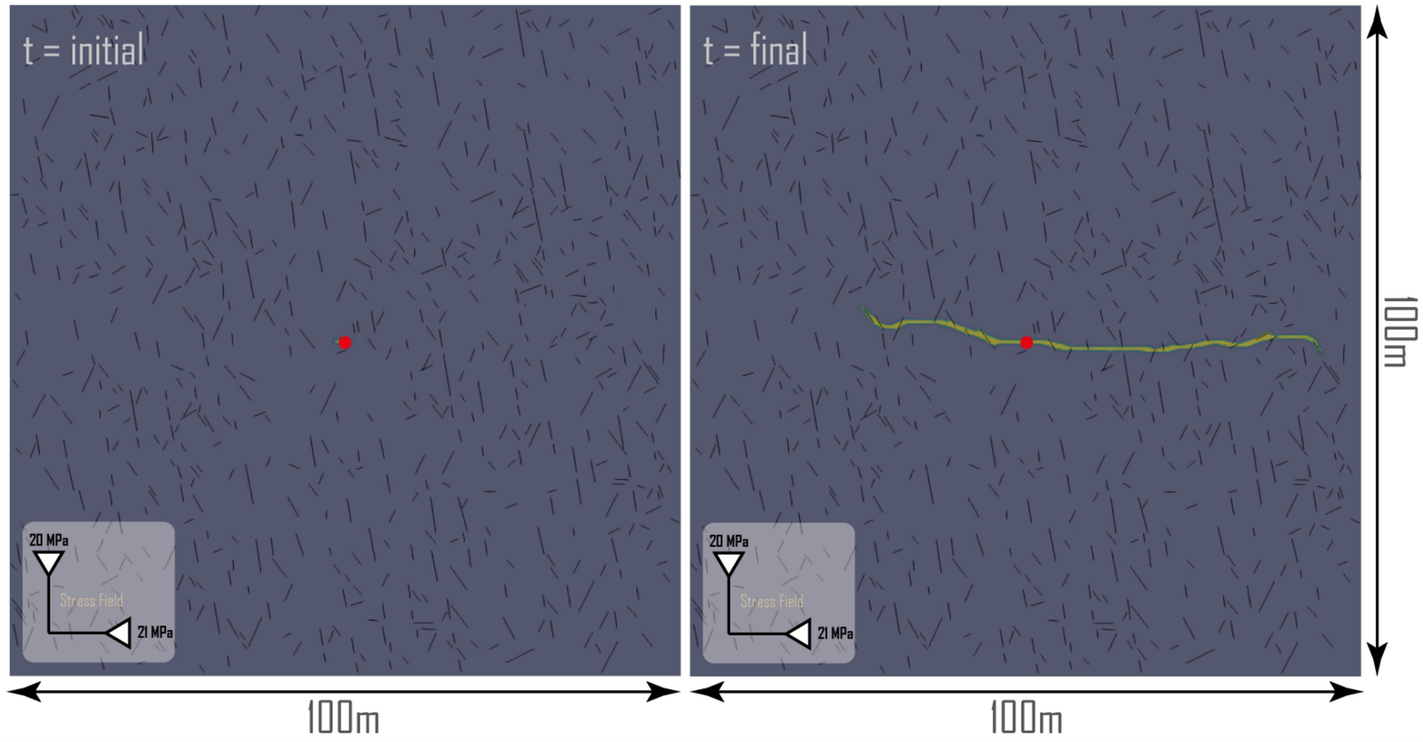

HF propagation plot

Ω + Γ Skarn: Sk02

Phase-field

HF propagation plot

Ω + Γ Skarn: Sk03

Phase-field

Figure 11.

a

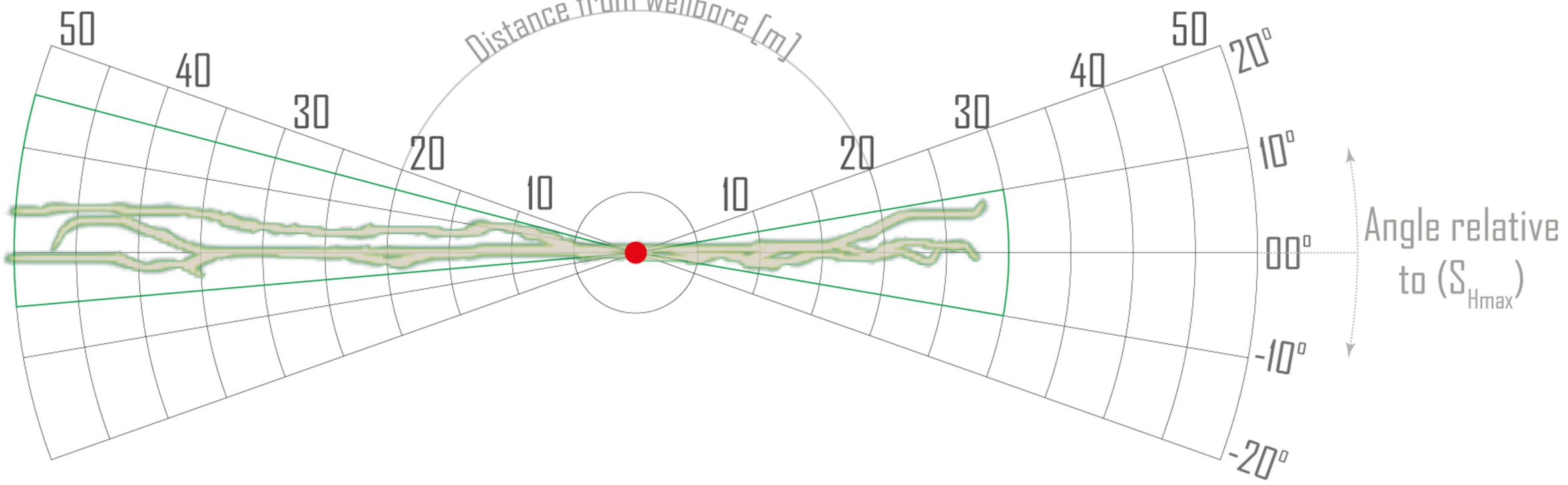
Distance from wellbore [m]
50
40
30
20
10
10
20
30
40
50
20°
10°
00°
-10°
-20°
Angle relative to (S_{Hmax})

b

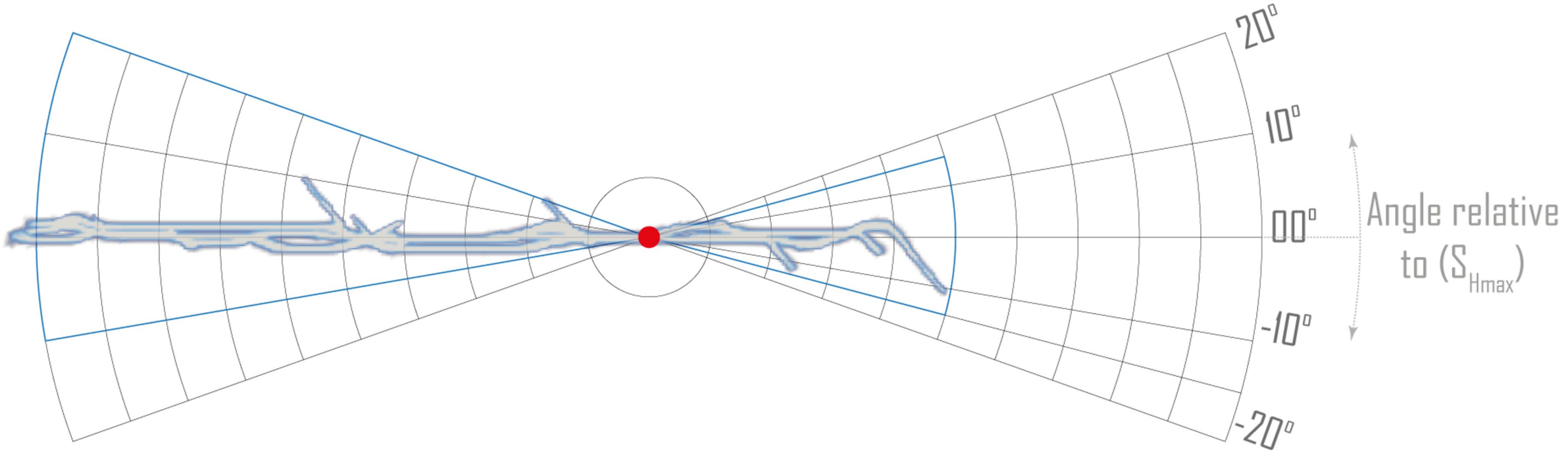
20°
10°
00°
-10°
-20°
Angle relative to (S_{Hmax})

c

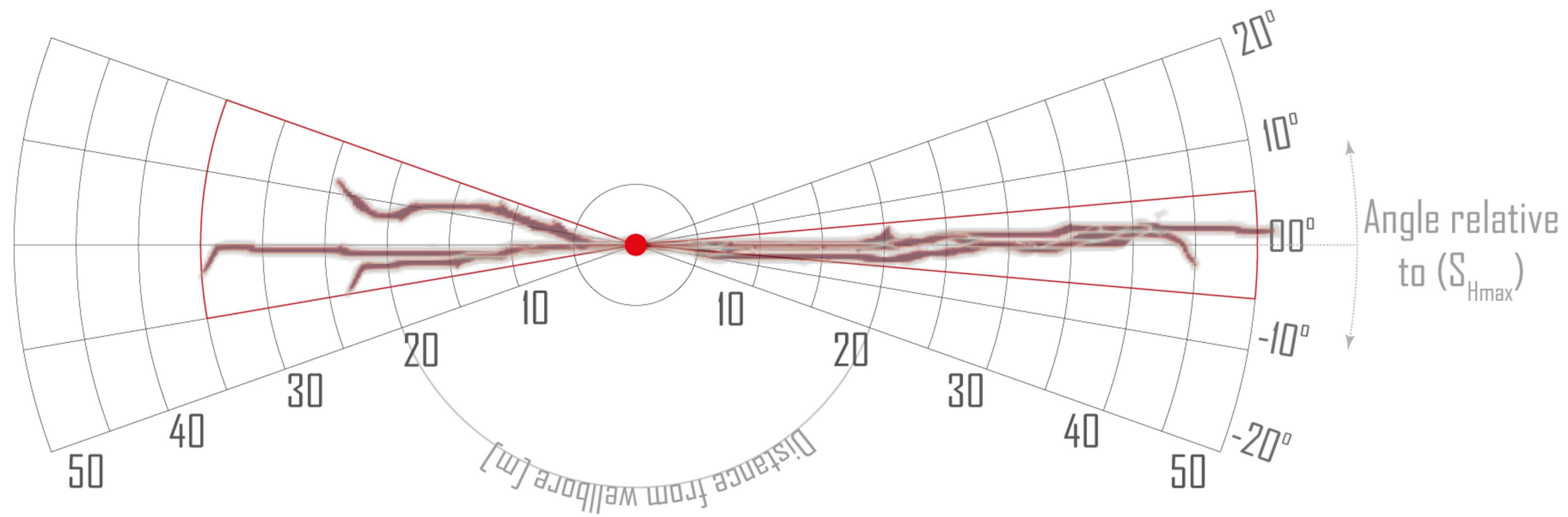
20°
10°
00°
-10°
-20°
Angle relative to (S_{Hmax})
50
40
30
20
10
10
20
30
40
50
Distance from wellbore [m]